UNIVERSITÀ DEGLI STUDI DI PADOVA

Dipartimento di Fisica e Astronomia "Galileo Galilei"

Erasmus Mundus Joint Master Degree in Nuclear Physics

Final Dissertation

Study for a toolbox probes for UGV platform in D&D operations

Thesis supervisor

Prof. Sandra Moretto

Thesis co-supervisor

Dr. Felix Pino

Candidate

Osama Ahmad

Academic Year 2021/2022

Abstract

The present thesis is a part of H2020 European project CLEANDEM. CLEANDEM plans to significantly improve Decommissioning and Dismantling (D&D) operations of Nuclear facilities by introducing some technological breakthrough while offering the possibility to deploy new methodologies. This thesis project work consisted of addressing the two key features of the CLEANDEM. These are gamma-ray spectrometry and neutron measurements using single detector for hotspot localization and radionuclide identification. It involves technologies which can be embedded on Unmanned Ground Vehicle (UGV) to enable the full remote non-destructive characterization in harsh environments, hence reducing human exposure to radiation. This included the development of probes addressing both the gamma spectroscopy and the gamma/neutron detection and source identification equipping the UGV platform. The systems were prepared and extensively tested with point-like gamma laboratory sources and ^{252}Cf gamma-neutron source. The study comprised of using two scintillators suitable for this purpose, a 2"x2" NaI(Tl) doped with ^{6}Li also known as NaIL, which is an inorganic scintillator and a 2"x2" EJ-309 which is an organic liquid scintillator both having with γ/ neutron discrimination capabilities.

NaIL proved to be an excellent candidate for gamma spectroscopy owing to its resolution 6.5% at 662 keV and gamma/thermal neutron discrimination capability. A quantity of interest known as Figure of Merit (FoM) which represents how well the gamma and neutrons are separated was determined to be 4.10 for NaIL. A preliminary study was also done by coupling EJ-309 with a PMT and a SiPM in order to study its response. EJ-309 has the capability to detect the fast neutrons and can be used a counter. The FoM for EJ-309 coupled with PMT and SiPM was found out to be 2.34 and 1.36 respectively.

After the characterisation, NaIL was used in the scope of operations of CLEANDEM. The first test consisted of studying it as a neutron counter using ^{252}Cf source with different materials like Graphite, Polyethylene and Teflon shielding the detector having different thicknesses for moderation. The best moderator with an optimal thickness of 6 cm was Polyethylene which can be used with NaIL in places having a high neutron contamination. The other major test performed was mounting the NaIL on a movable platform as a UGV prototype for remote localisation of the radioactivity hotspot and its identification. The mounted detection system was able to locate the radiation hotspot as well the identification of the source comprising the hotspot.

As an extension of the project, NaIL was further used for ambient dose estimation from the gamma-ray spectra obtained from it. This included extensive use of Monte Carlo simulations package called Geant4. It was an attempt to address one of the other key features of CLEANDEM which is online dose rate monitoring. The idea behind it was the conversion of gamma spectra obtained from NaIL into gamma fluence using the stripping matrix. The stripping matrix is constructed using Geant4 simulations having the detector geometry defined exactly as available in the laboratory. A GM counter was used to measure the gamma dose which was used as a control to the estimation of the ambient dose from the NaIL gamma spectra.

Acknowledgment

It is a genuine pleasure to express my deep sense of gratitude to Erasmus Mundus NucPhys program for providing me with such an amazing opportunity. I have been really fortunate to be a part of this program which not only allowed to participate in different universities across Europe but also provided insights into the research world. It has been two dynamic years filled with beautiful memories of classes, experiments, hard work and a lot of travelling.

I would like to start by thanking my supervisor Dr. Sandra Moretto for giving me the opportunity to do my master's thesis project at the National Institute of Nuclear Physics, Legnaro (INFN-LNL).

There are so many names that come to mind from my nuclear physics family while extending my gratitude. The first two "bhai's" who have been a constant companion in the last two dynamic years are Pathan and Harsh. Thank you for always being there. It would neither have been easy nor fun without you guys. Another very close person from the southern land of India who have been like an elder brother is Nithish "macha". I really cannot thank you enough for your valuable corrections for the thesis and your support throughout the last two years. I sincerely hope we collaborate on research work in future and continue to discuss science. I would like to thank my Spanish "hermano" and an amazing flatmate Marvin who kept me going and made sure to win the ice creams off the ping-pong. My "fra" Lorenzo who always took care that we talked work and life every evening after coming from Legnaro. Another "dost" Filippo who constantly stayed in touch and made Italy more welcoming. Thanks for for all the amazing dinners and inside jokes. I would like to extend my thanks to the "hombre" Gica and funny "young man" Godwin. Thank you guys for all the beautiful memories.

The last two years would not have been the same without my extended Erasmus family, "Habibi" Issam, "Choch" Marinella, "Hooligan" Maria, "Hermosa" Malen and "Petite" Lisa. I am going to miss you guys.

I would not have been here if it wasn't my family members in India whom I dearly missed in the last two years my mother, brother Abdul, Ayesha and Umar. Thank you for your support and understanding. The two most important people in my life to whom I would like to dedicate this work are my brother Wareed and my sister-in-law Zoya who always inspired me that the sky is the limit. Thank you for your patience and unconditional love. My accomplishments are as much as yours and I will try my best to make you all proud.

Last but not the least, I would like to convey my sincerest regards to my first "European" friend Manuel who made me feel welcome in this alien land and have always been a well-wisher. Thank you for everything.

Contents

List of Figures

List of Tables

List of acronyms

CLEANDEM	Cyber physicaL Equipment for unmAnned Nuclear DEcommissioning Measurements
UGV	Unmanned Ground Vehicle
DT	Digital Twin
PMT	Photomultiplier
CsI(Tl)	Cesium Iodide doped with Thallium
NaI(Tl)	Sodium Iodide doped with Thallium
CLLB	$Cs_2LiLaBr_6(Ce)$
BGO	$Bi_4Ge_3O_{12}$
FoM	Figure of Merit
SF	Spontaneous Fission
ASIC	Application-Specific Integrated Circuit
MC	Monte Carlo simulation
FPGA	Field Programmable Gate Array
PSD	Pulse Shape Discrimination
DPP	Digital Pulse Processing
ADC	Analog-to-Digital Converter
SiPM	Silicon Photomultiplier
SPAD	Single Photon Avalanche Diode
RGB	Red, Green, and Blue light
NUV	Near Ultraviolet Light
DCFD	Digital Constant Fraction Discrimination
INFN-LNL	National Institute of Nuclear Physics in Legnaro
PCB	Printed Circuit Boards

Chapter 1

Introduction

Radiation materials and radioactive sources are used in today's world in a variety of industries, including healthcare and diagnostics. They can be identified by their activity and the radiation types they emit, which can include gamma rays, alpha, neutrons, and beta particles [5]. The Nuclear Regulatory Commission of the United States classifies certain radioisotopes as Special Nuclear Materials (SNM), including ^{235}U, ^{233}U, and ^{239}Pu, as possible threats to humanity. Both civilian and military establishments use these materials, particularly nuclear power plants that produce electricity and nuclear propulsion vessels. Radiation monitoring is necessary to stop the spread of dangerous radiation. The expansion could be the result of illicit trafficking, faulty decommissioning of nuclear facilities, or nuclear disasters like Fukushima and Chernobyl.

The sensing technology could malfunction during a natural disaster, which would leave us in the dark. Since the dose exposition is unknown in these circumstances, mobile devices with embedded detectors are utilized to monitor or map the area without endangering human lives [5]. Due to their compact size and remotely controlled movements, which enable online evaluation of the activity and the precise position of the material, a UGV (Unmanned Ground Vehicle) or a UAV (Unmanned Aerial Vehicle) can represent the finest options for all the scenarios stated above [9]. The mobile detection devices are also employed for the upkeep of particle accelerators and the monitoring of nuclear plants in regions with high concentrations of naturally occurring radioactive materials.

Finding the source and detecting it are crucial in this type of radiation monitoring, but it is also highly useful to recognize the many radioisotopes that are having an impact on the area. Finding the hotspots and different radioisotopes in order to decommission and dismantle a specific site is one of the key goals of CLEANDEM. Due to the simultaneous detection and discrimination of gamma and neutrons (fast or thermal), it represents a novel approach for the detection and identification of radioactive materials in a specific area . Due to the fact that SNM (Special Nuclear Materials) can be shielded or hidden by a strong gamma background, this trait particularly enables the detection of SNM. 11 partners from four EU nations—Italy, France, Germany, and Spain—will work together on the project to deliver a cyber-physical system using an unmanned ground vehicle platform outfitted with cutting-edge radiological sensing probes. It will evaluate the region's radiological situation and keep an eye on D&D activities. This will produce a radiologically enhanced 3D digital twin of the scanned area that is completely detailed. Under the research and innovation program Horizon 2020, the EU Commission co-funds the project.

With the use of an unmanned ground vehicle (UGV) platform, the CLEANDEM (Cyber physicaL Equipment for unmAnned Nuclear DEcommissioning Measurements) project suggests a technological advance related to various Decommissioning and Dismantling (D&D) operational processes. It seeks to greatly enhance the procedures now used at various stages of (D&D) activities. This improvement will be made by addressing important technical roadblocks and associated challenges that are currently encountered during routine DD operations, initial radiological characterization of nuclear sites, and final characterization that will be performed at the end of the entire process. The goal of CLEANDEM is to deliver significant D&D achievements, and the UGV Platform's planned effects include time savings, cost savings, a reduction in the need for human intervention, increased worker and population safety, and environmental friendliness. An intensive testing and validation campaign that will be carried out in labs, in a simulated environment, and ultimately on the field will be used

to evaluate the effectiveness of the UGV Platform. With a complete commitment to non-destructive characterisation, CLEANDEM will concentrate on the creation of novel technological solutions based on cutting-edge building blocks. Current restrictions encountered during D&D operations will be resolved thanks to several key features, including remote localization of radiation hotspots, continuous and online dose rate monitoring, measurement of low-level alpha-beta contamination, gamma-ray spectrometry, and neutron measurements using single detectors.

CLEANDEM involves:

1. Technologies that can be integrated into unmanned ground vehicles (UGV) to provide complete remote non-destructive characterization under challenging conditions, hence lowering radiation exposure to people.

2. A Digital Twin (DT), which is a digital memory that allows one to save and update in real time the radiological state of a facility that is about to be decommissioned.

Decommissioning and Dismantling (D&D), which is also a well-known component of the nuclear ecosystem as known by decision-makers and populations, is one of the primary concerns for the nuclear sector in the future and is the driving force behind CLEANDEM. The topic has arisen as a result of the nuclear plants' advancing age. In fact, the nuclear business essentially expanded in the latter half of the 20th century despite the facilities' limited lifespans, which were initially projected to be no longer than 40 years for nuclear power plants (NPPs). Furthermore, the recent dramatic events at the Fukushima Nuclear Power Plant in Japan have generated a significant and unanticipated D&D application case. The Fukushima disaster has a long-term, global influence on nuclear activity, leading some nations to decide to quickly phase out nuclear power.

D&D operations will last for several decades and can be carried out in a wide range of configurations, including nuclear power plants, reprocessing facilities like the La Hague facility, which uses a number of intricate processes, nuclear fuel production facilities for uranium enrichment, research reactors, and specialized facilities found in research centers like the fast neutron reactor PHENIX at CEA Marcoule.

The primary goal of CLEANDEM is to create a fully functional set of tools that can be quickly and easily integrated into unmanned ground vehicles (UGVs) for use in various D&D and clean-up scenarios where different types of radiological characterization are required to obtain the best radiological information possible in order to support operations in the field. Ultimately, CLEANDEM will be able to:

- Improve operational effectiveness and to validate in during in-situ measurements,

- Improve the safety of operators as well as to reduce personnel dose rate,

- Enhance financial optimization (gain from the operational point of view on deconstruction sites),

- Improve the economical competitivity of companies.

The objectives of this thesis work in the frame of the CLEANDEM project are:
Gamma and neutron source spectroscopy identification. The second solution put forth is employed as a backpack detector for discrete radiological monitoring of critical areas in security applications. It is a double detection system built on a digital and quick acquisition that can discriminate gamma as well as neutron sources. For instance, between ^{60}Co, ^{137}Cs, ^{133}Ba and AmBe, ^{252}Cf, ^{238}U and ^{239}Pu. When the D&D program is operating in search mode or one of the other sensors on the UGV issues a radioactive alarm, the major usage will be the simultaneous detection of gamma and neutron sources. The source's identification enables the operator to better control subsequent intervention.
Since the system is typically used in a natural background setting, it must be tested in a hostile

environment situation to determine its limits. Additionally, the measuring technique needs to be re-defined in order to be compatible with the D&D process. In this project, a new prototype for the D&D application will be redesigned to be attached as an external probe to the UGV and tested while maintaining the detection technology capable of integrating the UGV for long-term environmental monitoring and performing a PSD (Pulse Shape Discrimination) between gamma and fast/thermal neutron signals.

Gamma and neutron hot spot characterization. A handheld device for the characterization of gamma and neutron hotspots discovered during the environment monitoring is the first technology that will be incorporated into the project. The concept is that in the event of a gamma or neutron alarm, the dual detection system will do a neutron gamma discrimination and a first gamma spectroscopic study without requesting the assistance of an operator, simply by extending a UGV arm where the hotspot is detected.

The system is based on new scintillator, the NaILi^6, a NaI scintillator doped with Lithium which has a high neutron cross section for thermal neutron capture ($\tilde{9}40$ bn) and also be able to provide a gamma spectroscopy with an energy resolution of an undoped NaI ($\tilde{7}\%$ @ 662 keV). These two characteristics are important to not lose the gamma characterization capability and adding the neutron detection capability.

In addition to the scintillator, the digital electronics with waveform analysis capabilities are also crucial. The PSD detection method is crucial for differentiating between neutron and gamma radiation. As part of the project, a fully functional system based on these two technologies is built and developed in a way that it can be mounted on a UGV arm and used in the field.

Identification and qualification of gamma and neutrons emitting radionuclides.Techniques for gamma-ray spectrometry and neutron detection are essential components in the context of nuclear operations, particularly during D&D interventions. Detecting the presence of particular radionuclides in a facility is the primary goal (actinides like plutonium or uranium, activation or fission products). The development of handheld probes that combine gamma and thermal neutron detection using a special detector and are compatible with DD applications has exciting new possibilities because to the appearance of novel scintillating materials like the NaIL(Tl) made by Saint Gobain.

Moreover an attempt to estimate the **Ambient Dose H*(10)** from the gamma spectra of the NaIL detector is also made in this thesis. This study is an extension of the project and is discussed in detail in the appendix. Dose rate is a crucial parameter for defining D&D operations to be carried out in an irradiating environment. In this thesis work, a new approach is used in order to estimate the Ambient dose H*(10) from the gamma spectra of the NaIL detector using stripping method. Dose rate measurement is essential for radiological mapping and therefore this study was done in order to exploit the dose estimation capability of NaIL. The estimated ambient dose was then compared with the Geiger counter in order to check how well the estimation works.

Chapter 2

Theoretical description

This chapter aims to introduce the reader to the concept of the scintillation detectors, the basic principles underlying their operation, along with the mechanisms. Following it, the fundamental principle of Photomultiplier tubes and Silicon Photomultiplier has been described in brief. In the last segment of this chapter, emphasis has been laid on the applicable measurements employed that relate to the analytical portion of this thesis work.

The subsequent chapters discusses the various detectors and probes that were studied and utilized for further experiments conducted in the course of the completion of this dissertation. However, to appreciate the motivation behind the selection of particular detectors used for this project, a certain degree of prerequisite understanding is required and hence from my side, a sincere effort has been made to acquaint the reader about the same in this chapter.

2.1   Scintillation detectors

Unquestionably, one of the most popular and commonly utilized particle detection tools in nuclear and particle physics today is the *scintillation* detector. It works primarily by taking use of the fact that some materials emit a short burst of light called a scintillation when they are exposed to radiation or nuclear particles. This light must be amplified using a device known as a photomultiplier tube (PMT) because its energy is relatively low. These scintillations can be transformed into electrical pulses, which can then be electronically examined and tallied to provide data on the radiation incidence. [2]
The scintillators have been around since 1903, when Crookes used them for the first time to detect particles. When α particles struck the *ZnS* screen that made up the instrument, weak scintillations were produced. They could be recognized with the naked eye under a microscope in a well-lit area. Despite being utilized by Gieger and Marsden in their well-known "α scattering" studies, it was tedious to use and never gained much popularity. The optical scintillators were swiftly supplanted when gaseous detectors were developed [2].
In 1944, around half a century later, Curran and Baker recreated the scintillators by using the then-recently invented photomultiplier tube in place of the human eye. Now, it was possible to count weak scintillations with accuracy and dependability on par with gaseous ionization devices. Due to this, the current electronic scintillation detector was created [2].
However, as there isn't a scintillation material that perfectly combines all the properties, choosing a scintillator involves giving up some features in favor of others. For instance, inorganic scintillators offer the best light output and linearity despite having a very poor temporal response. On the other hand, organic scintillators have a lower light production but a quicker time response. Additionally, the type of particle being detected affects the detector choice. Due to their high atomic number and density, inorganic scintillators are typically utilized for photon detection, while the hydrogen concentration in organic scintillators makes them suitable for the detection of fast neutrons [2].
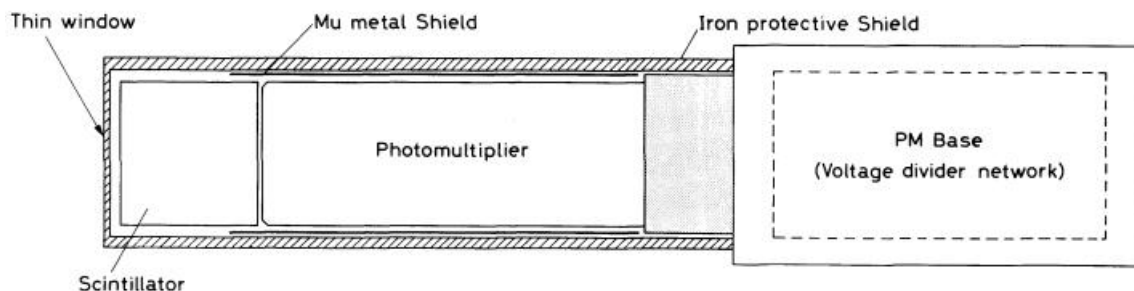
Figure 2.1: Schematic diagram of a scintillation counter. Figure taken from ref. [1]

2.1.1 General Characteristics

Figure 2.1 represents the basic elements of a scintillator detector. In most cases, a photomultiplier is optically attached to a scintillating substance, either directly or by a light guide. Light is produced as a result of the scintillator's atoms and molecules being excited by radiation as it travels through it. This light is passed to the photomultiplier tube (PMT), where it is changed into a weak current for photoelectrons, which is then amplified further by the system. An electronics system then analyzes the generated current signal.

The scintillator signal in general is capable of providing a variety of information. Some of its outstanding features are:

1. *Sensitivity to Energy*: The light output of a scintillator is directly proportional to the exciting energy since most scintillators behave in a nearly linear manner with respect to the energy deposited above a specific threshold energy. The amplitude of the final electrical signal will also be proportional to this energy because the photomultiplier is also a linear device. The scintillator functions as an energy spectrometer.

2. *Fast Time Response*: Scintillation detectors are fast instruments because they respond quickly and recover quickly compared to other detector types. This quicker response enables more accurate timing information to be gathered, such as the interval between two occurrences. Due to the shortened dead time and quick recovery time, scintillators may handle larger count rates.

3. *Pulse Shape Discrimination*: The shape of the emitted light pulses can be used to distinguish between various types of particles (radiation) using specific scintillators. This results from distinct fluorescence mechanisms being excited by particles with varying ionizing powers. Since it is the main topic of this thesis work, the approach is known as pulse-shape discrimination and will be covered in more detail later in the chapter.

Luminescence is a feature of scintillator materials. When exposed to specific types of energy (light, heat, radiation, etc.), luminescent materials absorb the energy and then re-emit it as visible light. The process is referred to as "*fluorescence*" if the re-emission takes place shortly after absorption (within 10^{-8}s). In the alternative, the process is known as "*phosphorescence*" or "*afterglow*" if re-emission is postponed because the excited state is metastable. Depending on the type of material, the phosphorescence delay period between absorption and re-emission might range from a few microseconds to hours. At present, six types of scintillator materials are used: organic crystals, organic liquids, plastics, inorganic crystals, gases and glasses. The following sections are dedicated to the discussion of organic scintillators (liquids) and inorganic crystals as they are relevant to the current thesis work.

2.1.2 Organic Scintillators

Aromatic hydrocarbon compounds with connected or condensed benzene-ring structures make up the organic scintillators. Their extremely quick decay times, which are on the scale of a few nanoseconds or less, are what set them apart.

Since the transitions in a single molecule's energy level structure are the source of the fluorescence process in organic scintillators, it is possible to see it from any given chemical species regardless of its physical state. Anthracene, for instance, exhibits fluorescence as a polycrystalline solid, a vapor, or a component in a multicomponent solution. The inorganic scintillators, in contrast, require a crystalline lattice as the foundation of the scintillation process.

An extensive category of organic scintillators is based on organic molecules with certain symmetry properties known as a π-electron structure. The π-electronic energy levels of these molecules are shown in figure 2.2.
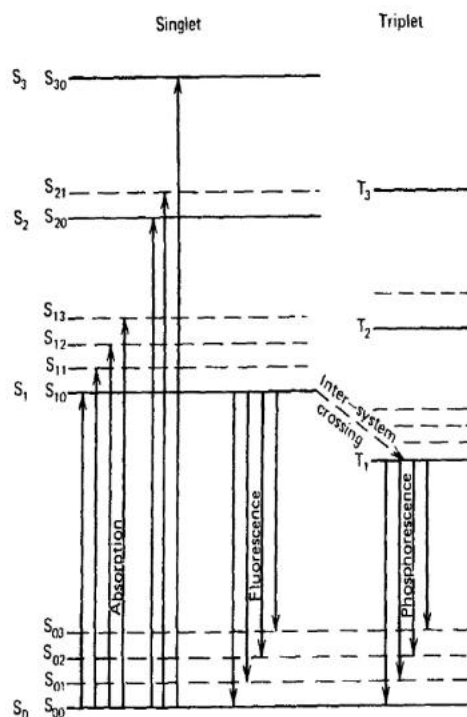
Figure 2.2: Energy levels of an organic molecule with π-electron structure.

The energy difference between S_0 and S_1 for organic scintillator molecules is 3 or 4 eV; distances between higher-lying states are typically smaller. Each of these electronic structures is separated into levels with much tighter spacing at the same time. In order to differentiate these vibrational states, a second subscript is added. Nearly all molecules at ambient temperature are in the S_{00} state because the distance between vibrational states is large compared to thermal energy (0.025 eV). In figure 2.2 the absorption of energy by the molecule is represented by the arrows going up. These processes represent the absorption of kinetic energy from a charged particle passing by in the instance of a scintillator.

When higher singlet electronic states are excited, internal conversion causes them to de-excite swiftly (on the order of picoseconds) to the S_1 electron state. Any state with an excess of vibrational energy, such as S_{11} or S_{12}, is likewise not in thermal balance with its neighbors and rapidly loses vibrational energy. Therefore, the overall result of the excitation process in a simple organic crystal is to rapidly generate a population of excited molecules in the S_{10} state.

When switching between the S_{10} state and one of the vibrational modes of the ground electronic state, the immediate fluorescence is released. The descending arrows in figure 2.2 indicate these transitions. The prompt fluorescence intensity at a time t after stimulation is given by [1],if τ is the fluorescence decay time for the S_{10}:

$$I = I_0 e^{-t/\tau} \tag{2.1}$$

The prompt scintillation component is relatively fast because τ is typically of the order of a few

nanoseconds in most of the organic scintillators.

The scintillation efficiency, which is the percentage of all incident particle energy that is transformed into visible light, is a key idea in the scintillation process. The ideal value for this would be as close to 1, but there are alternative molecular de-excitation modes that produce heat instead of light when they de-excite. Quenching refers to all of these de-excitation procedures without radiation release. It's crucial to avoid using liquid scintillators that are dissolved in organic contaminants, which reduce light output and introduce additional quenching mechanisms, during the production process.

2.1.3 Inorganic Scintillators

The primary inorganic scintillators are alkali halide crystals with a tiny activator impurity. The energy levels that the material's crystal lattice provides determine the scintillation mechanism. In materials that can be insulators or semiconductors, electrons only have discrete bands of energy available, as seen in figure 2.3. The valence band, which is the lowest band, is made up of electrons that are bound to lattice sites. The electrons with sufficient energy to move around the crystal are represented by the conduction band. The forbidden band, which is the last band, is an intermediate band in which electrons can never exist in a pure crystal. An electron may be promoted from the valence band to the conduction band as a result of energy absorption, leaving a hole in the valence band.
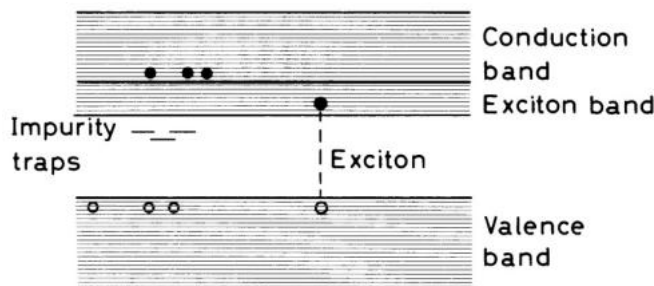
Figure 2.3: Energy band structure of a crystalline scintillator.

The emission of a photon to return the electron to the valence band in a pure crystal is an ineffective process. Additionally, because of how wide the gaps are, the photon that is created has an energy that is far too high to fall within the visible spectrum. Small amounts of impurities are therefore introduced to inorganic scintillators to enable the observation of photons in the visible range during the de-excitation process. The usual energy band structure of the pure crystal is altered by these impurities, which are also referred to as impurity traps or activators. The substance that is employed the most frequently is NaI(Tl), where Thallium (Tl) acts as an impurity activator. The other crystal that is now in use is CsI(Tl), where Tl is yet another impurity activator. Other crystals include CsF_2, Kl(Tl), CsI(Na), and Lil(Eu). $Bi_4Ge_3O_{12}$ (BGO), BaF_2, ZnS(Ag), ZnO(Ga), $CaWO_4$, and $CdWO_4$ are a few examples of non-alkali materials. As a result, there will be energy levels in the forbidden band that the electrons can pass through in order to de-excite and return to the valence band. The transition now produces photons in the visible range and serves as the catalyst for the scintillation process since the energy is lower than the energy of the complete prohibited band. The emission spectrum of the scintillator is determined by the energy structure of these luminescence or recombination sites in the crystal lattice.

2.2 Scintillation readout

The light emitted from the crystals (organic and inorganic) can be converted into electrical signal by means of two devices. These are discussed below in detail.

2.2.1 Photomultiplier Tube (PMT)

Electron tube devices called photomultipliers (PMs) transform light into a quantifiable electric current. Although they have a wide range of applications, they are incredibly sensitive and most frequently used in nuclear and high-energy physics in conjunction with scintillation detectors.

The components of a conventional photomultiplier are an anode, dynodes, and photocathode. The photoelectric effect occurs when light from the scintillator strikes the photocathode, creating photoelectrons that are then driven to the first dynode by a potential difference. The amplification of the electrons is on the order of 107 when the photoelectrons impact the dynode, causing additional electrons to be emitted, which are then propelled to the next dynode, and so on. Finally, the photomultiplier's anode gathers all of these electrons into a current that is prepared to be processed by the electronic nuclear chain [2].

The majority of PMTs carry out this charge amplification in a relatively linear fashion, resulting in an output pulse at the anode that is proportional to the number of photoelectrons throughout a broad amplitude range. The original light pulse's timing information is also preserved to a large extent. When a pulse of extremely short duration is emitted through a typical PMT, after a delay of 20–50 ns, the PMT produces an electron pulse with a temporal width of a few ns.

2.2.2 Silicon Photomultiplier (SiPM)

In the literature, silicon photomultipliers are often referred to as "SiPMs", and they are solid-state, single-photon-sensitive devices built on a silicon substrate with a Single-photon avalanche diode (SPAD) placed on it. Every SPAD in the SiPM operates in the Geiger mode and is connected to the others by a quenching resistor made of metal or polysilicon. SiPMs may generate signals with a dynamic range from a single photon to 1000 photons for a device with just a square millimeter area, even if the device operates in digital/switching mode. This is feasible because all the microcells are read in parallel. It is used in all applications where low light/radiation levels must be evaluated and quantified with great precision. It is based on reversed biased p-n diodes and can directly detect light from near ultra violet to near infrared. An electron has enough energy to go from the valence band to the conduction band when a photon passes through silicon, transferring its energy to a bonded electron. This results in the formation of an electron-hole pair. In the case of reverse bias, an electric field is created towards the depletion zone, causing the charge to accelerate in the direction of the anode (holes), where secondary charge pairs are produced when the charge has enough kinetic energy. In this manner, a single photon absorbed by the silicon will start an ionization cascade that spreads across the silicon volume, causing the silicon to degrade and turn into a conductive material that will magnify the electron-hole pair into a macroscopic current flow. In a reverse-biased photodiode, an absorbed photon will therefore be equivalent to a flow of current; this process is analogous to the ionization discharge that takes place in a Geiger-Muller Tube. A series of resistors are used to quench or stop the current flowing through the silicon. The sensor is then prepared to detect a new photon after the diode recharges back to the bias voltage, limits the breakdown current of the diode, decreases the reverse voltage, and stops the avalanche [18].

The response will always be equal to the interaction of a single photon if many photons are absorbed by the SPAD (Single Photon Avalanche Diode) at the same time. The SiPM, which can independently complete the cycle of breakdown, avalanche, quench, and recharge of the bias to a value above the breakdown voltage, is made up of a dense array of independent SPAD sensors or microcells that each have their own quenching resistor (Fig. 3.3). The other cells are prepared to detect additional photons when the avalanche process is taking place in one cell [18].

The SPAD's current increases due to the avalanche, which causes the voltage at the quenching resistor to drop. As a result, the voltage at the SPAD decreases until it reaches the breakdown voltage, at which point the bias is restored through the same resistor with a time constant or recovery time. The avalanche's rise time is comparable to the SiPM pulse's rise time, and the microcell recharge time constant controls the pulse's decay duration, which is the sensor's recovery time.

Because the area of the microcell affects both the capacitance and the recovery time, larger microcell sizes result in longer recovery times. Additionally, when the charge increases with microcell size, the amplitude of the pulses for each event increases, necessitating less amplification for each event.
The energy of the event determines how many visible photons are produced in the scintillator. All of these visible photons are subsequently absorbed by part of the microcells in the SiPM, resulting in a flow of current. As a result, the total charge produced in the SiPM is equal to the energy of the event. Thermal electrons generated inside the volume of a SiPM are the main source of noise in that device. These events, known as dark counts, are influenced by the temperature of the SiPM. When carriers are accelerated in a high field, photons in the infrared range can be created. Later, these photons can trigger nearby microcells. Optical crosstalk is another sort of noise that can occur [18].

2.2.3   Pulse shape discrimination in scintillators

The prompt fluorescence in organic scintillators accounts for the majority of the scintillation light that has been detected. There is also a component with a longer lifetime that correlates to delayed fluorescence. While the slow component normally decays over several hundred nanoseconds, the prompt component typically decays over a few nanoseconds. Although it doesn't contribute much to light output, the slow component has a special quality. **The kind of exciting particle often determines the amount of light that occurs in the slow component**. By taking advantage of this delayed component quality, it is possible to distinguish between different types of particles (such as neutrons, gammas, heavy ions, etc.) that provide the same amount of energy to the detector. When using organic scintillators as neutron detectors, this method, known as **Pulse Shape Discrimination (PSD)**, is frequently utilized to remove the gamma-ray-induced events [1].
When long-lived triplet states (T1) are excited along the path of the ionizing particle, the slow scintillation component results. When two of these excited molecules interact biomolecularly, the resultant molecules can have one in the lowest singlet state (S_1) and the other in the ground state. The delayed fluorescence results from the singlet state molecule's ability to de-excite after that. As a result, the amount of delayed fluorescence that can be produced by a single ionizing particle must be proportional to both the density of excited molecules in the triplet state (T_1) and the density of molecules in the singlet state (S_1). It can be inferred that the rate of energy energy loss along the route $\left(\frac{dE}{dx}\right)$ is proportional to the delay fluorescence because the excitation of the molecules to the (S_1) state simultaneously depends on the linear energy loss of the ionizing particle. This explains why heavier particles exhibit delayed light with a higher intensity [1,17].
Certain organic scintillators are preferred for PSD due to the significant variations in the relative slow component caused by various radiation types. Because there is hydrogen in the organic scintillator, which causes protons to emit and ionize the material, fast neutrons are detected through elastic collision. The Compton effect explains why the detection of gammas results in a less intense delay fluorescence than the detection of fast neutrons, but photons are detected by electrons that are created as a result of this effect.

2.2.4   Figure of Merit (FoM)

Integrating the charge over two separate times is the technique used for pulse shape discrimination. It focuses on integrating the charge of the pulses over two time scales—a short time scale and a long time scale. For pulses with a common shape, the ratio of these two signals will be constant, which indicates that the ratio of these two-charge integrations will hardly be the same for each kind of particle 2.2. With this in mind, the **Figure of Merit (FoM)**, a quantity that describes the system's discrimination for various sorts of particles, can be used to measure the performance of the system's discrimination [1].
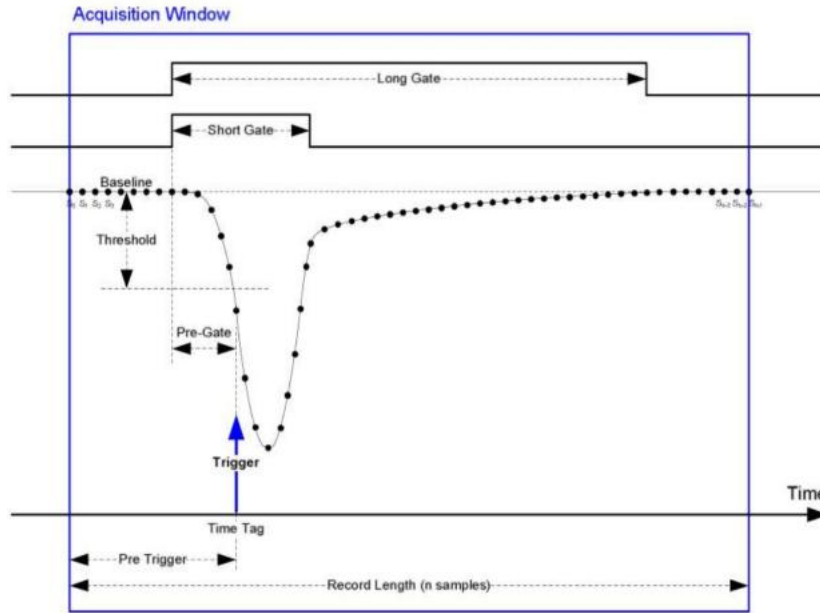
Figure 2.4: Acquisition parameters of a typical sample signal. Long gate and short gate are the two important parameters in PSD.

$$\text{PSD} = \frac{Q_{\text{long}} - Q_{\text{short}}}{Q_{\text{long}}} \tag{2.2}$$

By first generating a histogram that comprises the ratio between the two charge integrations of each pulse, the Figure of Merit parameter can be derived 2.3. This will result in a histogram, often known as a PSD plot and as seen in figure 2.5. Two events are seen, each of which indicates a particular kind of particle found in the same experiment (e.g. photons and neutrons). The following equation is used to determine the FoM after the histogram has been produced:

$$\text{FoM} = \frac{X}{W_A + W_B} = \frac{X_B - X_A}{W_A + W_B} \tag{2.3}$$

where X_B, X_A represents the centroids of the peaks, and W_B, W_A represents the Full Width at Half Maximum (FWHM), A and B represent the two different types of particles. The system discrimination is improved by a bigger FoM value. A good discrimination is considered to have a score of more than 1, and a value of more than 1.27 indicates that full discrimination has been achieved. This value of 1.27 is derived from the centroids' difference, which is 3σ; as a result, the FoM becomes FoM = 3σ / 2.35σ = 1.27.
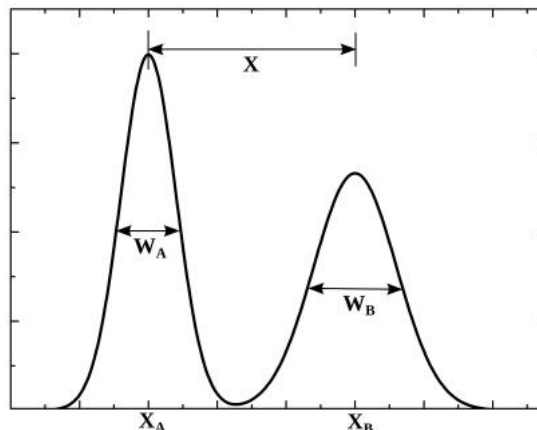
Figure 2.5: Representation of the FoM for PSD plot. [17]

2.3 Interaction of radiation with matter

2.3.1 Interaction of Photons with matter

Although there are numerous known gamma ray interaction mechanisms in matter, only three primary types—photoelectric absorption, Compton scattering, and pair production—play a significant part in radiation measurements. All of these processes result in the conversion of gamma-ray photon energy to electron energy, either partially or entirely. They cause abrupt and sudden changes in the gamma-ray photon history, with the photon either completely disappearing or being scattered via a significant angle.
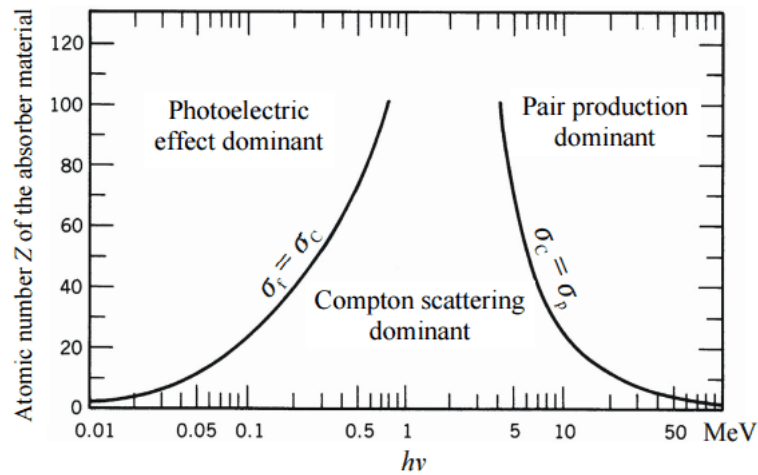
Figure 2.6: The relative importance of the three major types of gamma-ray interaction. The lines show the values of Z and hν for which the two neighboring effects are just equal. Picture taken from [1]

When the energy is less than 0.1 MeV, the photoelectric absorption takes over. In the energy range of 0.1 to 10 MeV, Compton scattering predominates, while pair formation predominates above 10 MeV.

2.3.2 Interaction of Neutrons with matter

Neutrons do not carry a charge, just as gamma rays, hence they cannot interact with matter through the coulomb force. Neutrons can pass through several centimeters of matter without interacting in any way, making them completely invisible to a detector of typical size. When a neutron interacts, it does so with the absorbing substance's nucleus. The neutron may completely vanish and be replaced by one or more secondary radiations as a result of the contact, or else its energy or direction may be drastically altered.

With increasing neutron energy, there is a significant change in the relative probability of the various types of neutron interactions. Since the detectors used in this experiment are capable of detecting fast and thermal neutrons, we will talk about their interaction here. Table 2.1 represents the classification of neutrons based on their energies.

Neutron	Energy
Cold	< 1 meV
Thermal	< 0.5 eV
Epithermal	0.5 eV - 50 keV
Fast	> 50 keV
Fast (medium energy)	> 1 MeV
Fast (high energy)	> 10 MeV

Table 2.1: Classification of neutrons based on energy

With rising neutron energy, the likelihood of the majority of neutron-induced processes that could be useful in detectors decreases sharply. The relevance of scattering increases due to the neutron's ability to convey a significant amount of energy in a single collision, but this also means that it becomes more important. Recoil nuclei, which have accumulated a measurable amount of energy from neutron collisions, are the source of the secondary radiations. The neutron loses energy and is subsequently regulated or slowed down at each scattering location. The neutron can lose up to all of its energy in a single encounter with a hydrogen nucleus, making hydrogen the most effective moderator. It is suggested to use liquid scintillators for neutron detection. They can be employed in mixed-particle radiation fields when pulse shape discrimination (PSD) techniques are used to separate pulses produced by various incident particles because they are sensitive to fast neutrons, which are primarily detected by elastic scattering with hydrogen. In this work, EJ-309 liquid scintillator is used for gamma and fast neutron detection. A comparative study is also performed by coupling it to a PMT and a SiPM.

Thermal neutron interactions are neutron-induced processes that can produce secondary radiations with enough energy to be directly observed. As a result of the low neutron energy of the incoming nuclei, all such reactions require a positive Q-value to be energetically feasible. Reactions such as (n, α), (n,p), and $(n, \text{fission})$ are of high importance in detectors because the secondary radiations are charged particles. The other detector being used for thermal neutron detection is NaI doped with ^{6}Li (NaIL). The doping of NaI crystal with ^{6}Li makes the detection of thermal neutrons possible as the reaction $n + {}^6\text{Li} \rightarrow \alpha + {}^3\text{H}$ has a high cross section for lower energies of neutrons (940.4 barn at 0.0253 eV).

Chapter 3

Experimental details

3.1 Inorganic and organic scintillators

The instrumentation that was used to characterize and test the detectors is covered in this chapter. There is also discussion of the uses for both inorganic and organic scintillators. The characteristics of the sources used for the testing as well as the electronic chain used for the readout are given. The simulation carried out to support the experimental data is explained in the latter section of this chapter.

Inorganic Scintillator: NaIL

For both gamma-ray and neutron detection, NaIL is a superb scintillation material. It is co-doped with ^{6}Li, which significantly improves the efficiency of thermal neutron detection to the most well-known gamma-ray scintillator ($n_{th} + {}^6Li \longrightarrow \alpha + {}^3H$). It is doped with ^{6}Li, having enrichment of 95%. Standard NaI(Tl) crystal's scintillation characteristics are unaffected by doping with ^{6}Li of NaI. The sodium iodide crystal [NaI(Tl+Li)], also known as NaILTM, has outstanding PSD [FoM = 3.0] [3] and is capable of detecting thermal neutrons and gamma radiation in a single crystal. Figure 3.1 represents a picture of the NaIL used in the lab.
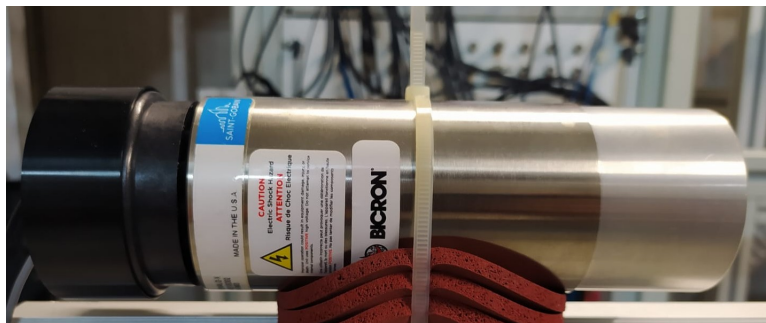
Figure 3.1: 2"*2" NaIL used in lab.

Advantages

1. NaIL is a great option for area monitoring and has a detection effectiveness of up to 57% for thermal neutrons.

2. Uniquely NaIL is able to offer both gamma and neutron detectors in big volumes with a single material at a cheap cost per volume.

3. Large NaI crystals can be grown quickly and cheaply.

4. For neutron attenuation, sodium and iodine are only marginally competitive with ^{6}Li.

5. It is possible to attain neutron detection capabilities comparable to those of ^{3}He, CLYC, or CLLB detectors at a lower cost by using low Li concentrations and large thicknesses.

6. Gamma ray spectral detection is improved by large volume detectors. There is no longer a need to compromise on the detectability of one species to be efficient for the other.

Density [g/cm^3]	3.66
Wavelength of emission max. [nm]	419
Primary decay time [ns]	240 ns, 1.4 µs, 230ns, 1.1µs
Light yield [photons/keV]	35

Table 3.1: Material Properties for NaIL [16]

Pulse shape discrimination makes it simple to discriminate between neutrons and gamma rays (PSD). Gamma ray scintillation pulses are longer than neutron reaction pulses when Li is included in the NaI matrix. Simple PSD techniques produce total separation with a stunning effect.

Organic Scintillator: EJ-309

As an alternative to the more widely used low-flash point PSD liquid scintillators based on the solvent xylene, EJ-309 is a liquid organic scintillator. It reduces the fire risk associated with liquid scintillators with low flash points thanks to its 144°C flash point. Although EJ-309 has slightly worse PSD characteristics than EJ-301, it has a number of chemical characteristics that make it a good choice for application in challenging environmental settings. High flash point, low vapor pressure, low chemical toxicity, and compatibility with cast acrylic plastics are some of these characteristics. As EJ-309B, EJ-309 is also offered with natural boron added. A picture of the EJ-309 liquid scintillator is shown in 3.2
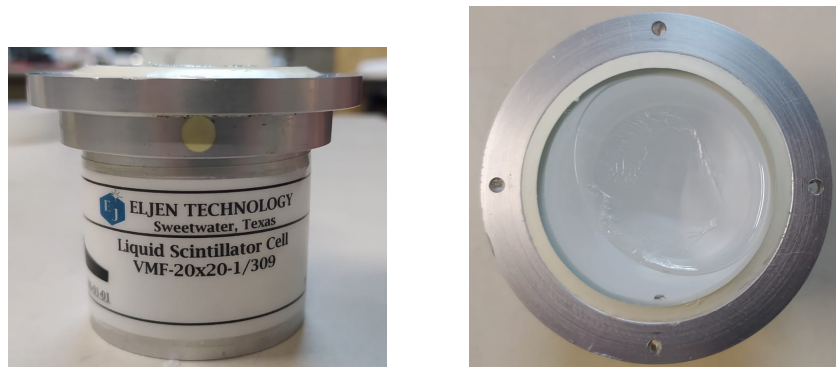
Figure 3.2: 2"*2" EJ-309 liquid scintillator side (left) and the top (right) view. This cell can be coupled to a PMT and a SiPM.

With the right PMTs and SiPM, EJ-309 can be read out in a number of geometries to get the best timing and neutron gamma separation via PSD.

Properties	EJ-309
Light Output (% Anthracene)	80
Scintillation Efficiency(photons/1 MeV e⁻)	12300
Wavelength of Maximum Emission (nm)	424
No. of H Atoms per cm^3 (x10^{22})	5.43
No. of C Atoms per cm^3 (x10^{22})	4.35
No. of Electrons per cm^3 (x10^{23})	3.16
Decay Time, Short Component (ns)	~ 3.5

Table 3.2: Main Characteristics of EJ-309 [14]

3.2 Electronics

In nuclear physics applications, the Front End Electronics' job is to collect the electrical charge pulses produced by a detector, separate out the amounts of interest, and transform them into a digital representation. A computer will then gather, store, and evaluate these data. The particle energy (proportional to the charge released by the particle in the detector) and time of arrival are relevant quantities in the majority of applications. In some cases, however, the acquisition is limited to pulse counting, which is actually a "selective" counting in which one or more energy intervals or other criteria are used to determine which particles must be counted. As in our case, the γ-n discrimination is based on a detector response variation stimulated by a gamma or a neutron; this variation leads to a different rise and/or decay time of the pulse. In some other situations, it is necessary to determine the type of the particle by means of the pulse shape. Digital logic units that perform (anti)coincidences, generate triggers, vetoes, and other signals that take into account the correlation between various channels are typically used to complete the acquisition system. These signals may also provide additional information, such as the particle position or trajectory.

Today, it is possible to construct acquisition systems in which the Analog to Digital conversion takes place as close to the detector as possible because to the availability of very quick and highly accurate flash ADCs. The information loss can theoretically be minimized using this acquisition system. In reality, uncertainties resulting from quantization noise and other types of electronic noise will have an impact on the acquisition.

In this section, the different components of electronic chain are discussed that were employed during this thesis work.

Photomultiplier Tube (PMT)

The photomultipliers used in this work are:

- HAMAMATSU H1949-51 which was coupled with EJ-309. The optimal voltage at which this PMT was operated is -1500 V. [44]

- HAMAMATSU E1198-07 which comes already assembled with NaIL. The optimal voltage for this PMT is +1150 V. [43]

Figure 3.3 shows the H1949-51 PMT which was coupled to EJ-309 and E1198-07 PMT coupled with the NaIL crystal.
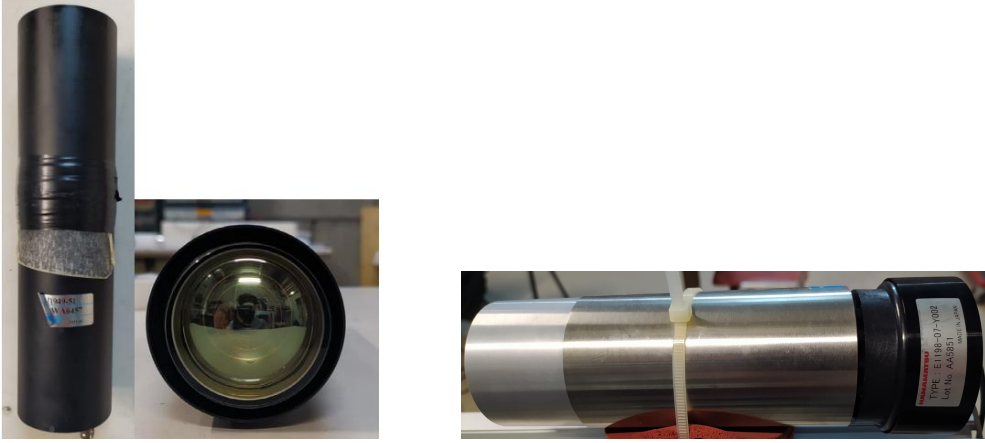
Figure 3.3: H1949-51 PMT (left) with over and front view and the E1198-07 PMT coupled with the NaIL crystal (right).

Silicon Photomulitplier (SiPM)

The SiPM used in this work is from AdvanSiD which is sensible to the ultraviolet light (NUV-SiPM). Each SiPM array is composed of 16 cells, and each cell has 1000 microcells. A picture of the 4x4 SiPM used is shown in 3.4. The main characteristic is shown in table 3.3.
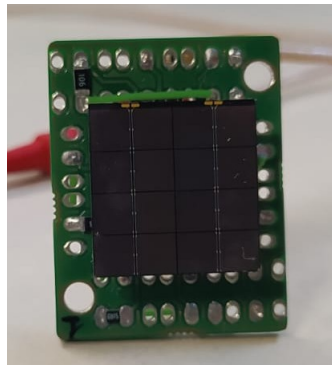
Figure 3.4: 4x4 NUV SiPM array.

NUV-SiPMs	Properties
Size	16.88 x 17.43 mm^2
Channels	16
SiPMs size	4x4 mm^2
Micro-cell size	40x40 μm^2
Cell fill-factor[1]	60%
Photon detection efficiency	43% at 420 nm
Typical breakdown voltage	26V
Silicon technology	P-on-N
Dark Count Rate	< 100kHz/mm^2@4VOV
Gain	3.6 x 10^6

Table 3.3: Main characteristics of the NUV-SiPM [15]

---

[1]The fill factor refers to the percentage of the SiPM sensor area that is sensitive to the light.
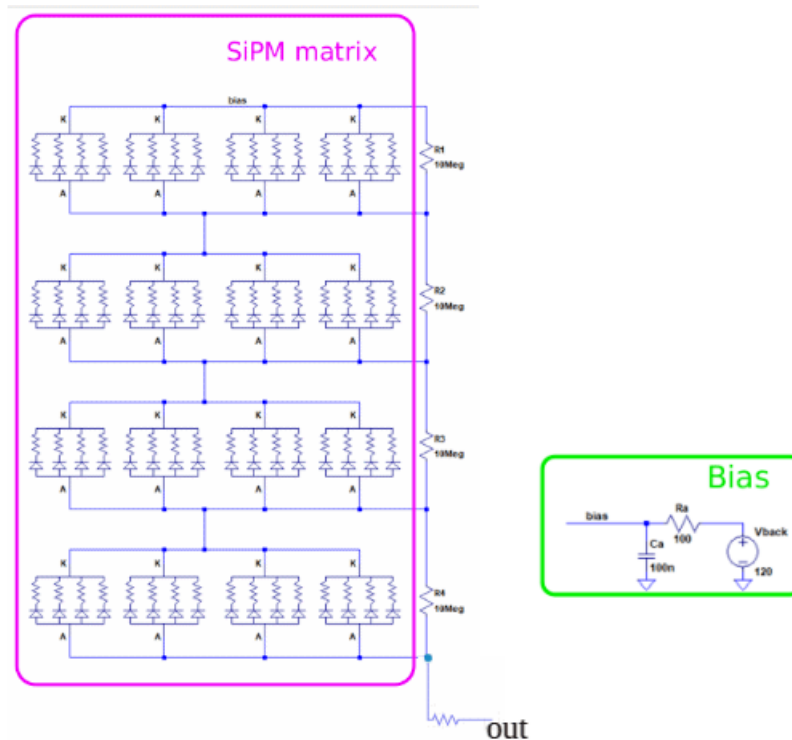
Figure 3.5: Circuit diagram of the SiPM array and the bias supply

3.2.1 Read-out board for the SiPM 4x4 arrays

TThe SiPM pulses must have an increase in amplitude while maintaining a constant pulse decay time because the PSD discrimination depends on this. A board that satisfies this condition was created by the Industrial Engineering University group at the University of Trento. It responds to two primary demands: In addition to providing the bias voltage and connecting the 16 pixels of the SiPM array, it also performs the amplification of the signal that is received from the anode. It is best to set up the readout of the SiPM and bias supply in a sequence of four sets connected in parallel, each set consisting of four single SiPMs connected in series; this will produce a cumulative signal with good amplitude and timing characteristics. This also makes it possible to efficiently manage the delivery of the necessary bias voltage to each pixel. The SiPM array and bias supply circuit diagram is shown in Figure 3.5. The SiPM array's microcells are made up of photodiodes with quench resistors and summed output.

3.2.2 High Voltage Supply

The CAEN model V6533M power supply module was used to provide high voltage to the following PMTs: H1949-51 PMT, coupled to EJ-309 (-1500V), E1198-07 PMT, coupled to NaIL (+1150V), and SiPM (-122V), as illustrated in figure 3.6, type VME[1] 6U. It is a module that houses six high voltage power supply channels with a 0 to 4kV energy range. The other three channels have positive output polarity, whereas three of the channels have negative output polarity. An overvoltage or undervoltage alarm alerts the user when the output voltage deviates from the preset value, and if the current exceeds the preset limit, an overcurrent detection occurs. In either case, the system cuts off after a preset amount of time. It is possible to set the parameters and operate this module remotely because it can be controlled from a computer (through a USB port) [13].

---

[1]VME means VERSA Module Eurocard, and corresponds to a standard data transfer architecture of the International Electrotechnical Commission

Figure 3.6: Power Supply Module CAEN model V6533M
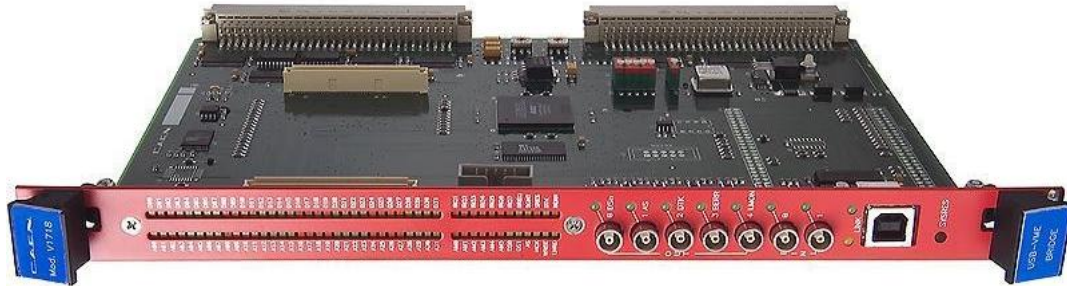
Figure 3.7: USB Port CAEN model V1718

3.2.3   USB Port (Controller)

The optical link bridge employed for this thesis project is the CAEN model V1718, which is depicted in figure 3.7. Its function is to connect the computer to the other nuclear electronic modules. It operates at a 30 MB/s speed. The controller V1718 uses a library of particular instructions for each module in the electronic chain to translate straightforward commands into VMEbus language. An optical fiber cable is used to connect the computer to the module. There are two input channels and five output channels in the module [13].

A small micro crate (model VME8004B) created by the CAEN company powered the Power Supply Module and the USB Port.

3.2.4   Waveform digitizer

The digitizer's job is to take in analog signals, convert them to digital form via converters, and then deliver the digitized samples to a buffer where they can be preserved and processed by a computer. Different modules are required in traditional digitizers in order to process the signal before the information can be retrieved. It is necessary to pre-amplify, split, delay, discriminate, and then transform the signals to digital signals. This module chain costs extra since it takes up more room. Furthermore, there is some distortion, loss of linearity, and attenuation as a result of the several processes the signals go through. The number of modules must be decreased in order to solve these issues.

In many different physics applications, waveform digitizers have recently gained popularity for reading out radiation detectors. The traditional analog electronics will be replaced by a fully digital approach, in which the detector output—with or without a preamplifier, depending on the type of detector—is connected directly to the digitizer input. In multi-parametric acquisition systems, where the analysis takes into account several quantities and characteristics including energy, pulse shape, and timing, this method is extremely advantageous. In reality, with the help of Digital Pulse Processing (DPP), it is now possible to use specialized online algorithms to extract relevant data from the raw waveform (usually in FGPAs). The digitizer may implement the many functions of the vintage TDC, QDC, Peak Sensing ADC, discriminator, and other analog and logic modules using DPP methods in "one single box". Additionally, because the complete waveform is only utilized for debugging, the DPP enables the digital readout to be sustainable in terms of data flow. As a result, a "multi parametric, all-in-one digital DAQ for physics applications" is produced.
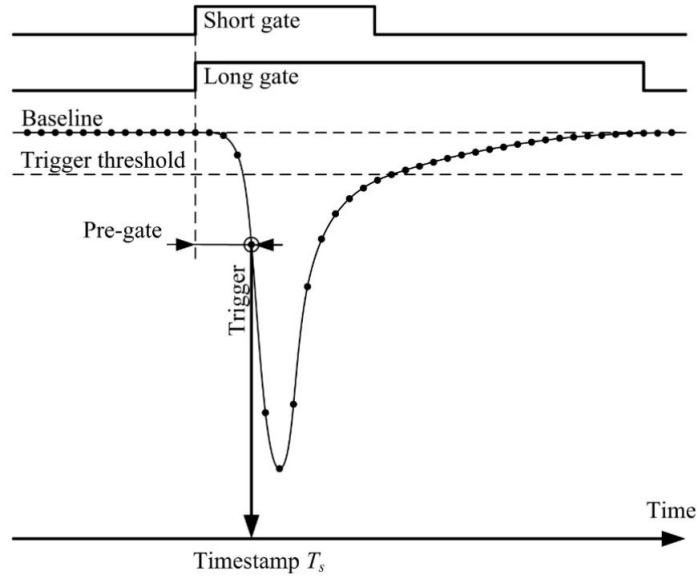
Figure 3.8: Acquisition parameters on a digitized pulse. Figure taken from [24]

The analog-to-digital conversion is carried out constantly in the waveform digitizer, and when a trigger event exceeds the threshold, a specified number of samples are kept in the buffer's memory. Two overlapping windows will be created and, as a result, two separate events will be stored in the buffers if a trigger happens while some acquired samples are being saved from another event. High counting rates may be measured using this, and unlike standard digitizers, there is no downtime or loss of events.

The algorithm used in the FGPA in this study generates the timestand, the baseline, the whole (Q_{long}) and partial (Q_{short}) integration charges for each triggered event. An input level with no noise or variations is represented by the baseline. The baseline is subtracted from the integration before the events are put in the buffer. The integration is the total of the samples found within the integration window. Adjustable factors include the pregate, which affects trigger location, and the integration window (Gate width). An example of a pulse with movable parameters is shown in Figure 3.8. The integration values can be used to determine the discrimination parameters.

$$\text{PSD} = \frac{Q_{long} - Q_{short}}{Q_{long}} = \frac{Q_{tail}}{Q_{total}} \tag{3.1}$$

Since the pulse tail of a fast neutron is fatter than the tail of a gamma ray, the PSD parameter for a fast neutron is bigger than that of a gamma ray. The PSD represents the fraction of delay fluorescence [17, 24].

In this work, two types of digitizers were used, the CAEN DT5725 which is a desktop module with 8 input channels, and the RedPitaya STEMLAB 125-14 (3.9) which is a portable light digitizer with two input channels, this digitizer is also installed in the DRAGON project, due to its lightweight and low power consumption. Owing to its these characteristics and portability, it was also employed for dynamic measurements. The main characteristics of these three digitizers is shown in table 3.4.

3.3   Data Acquisition System

The ABCD data acquisition (DAQ) system was employed throughout the project. This product was created for the C-BORD project [2]. This DAQ system is a brand-new distributed data acquisition

---

[2]Effective Container Inspection at BORDer Control Points

Figure 3.9: Left CAEN DT5725 and right RedPitaya STEMLAB 125-14 [12, 13]

	DT5725	**SETMLAB 125-14**
Dimension	154x50x164 mm^3 Desktop Module 680 g	70x15x100 mm^3 Portable 200 g
Analog input	8 ch. Impedance 50 Ohm	2 ch. Impedance 50 Ohm
Scale voltage range	0.5 or 2 Vpp	1 Vpp
ADC resolution	14 bits	14 bits
Sample rate	250 MS/s	125 MS/s
Connectivity	USB and Optical Link Controller	Ethernet, USB and WIFI
Power consumption	2 A, 12 V	2 A, 5 V

Table 3.4: Table representing the characteristics of the digitizers employed.

system with online analysis capabilities for digitized signals. The task of reading the ADC data from the digitizer is performed by a DAQ, which also provides controls for high voltage, power supplies, temperature, etc. The new DAQ model offers a system with all the processes separated, where the processes can be executed separately on other computers, preventing computing burden. This is different from conventional DAQ systems, which run only on one compute restricted by the hardware of the computer. The processes, which are known as servers, operate separately, giving them a flexible function because they can be activated, deactivated, or adjusted without affecting the system as a whole. Through the network socket, the processes are able to communicate with one another [25]. Each process works for a particular task, for example:

1. **ABCD** $\rightarrow$ Server that allows the communication with the CAEN digitizer

2. **HIVO** $\rightarrow$ where the High Voltage can be controlled

3. **LMNO** $\rightarrow$ send the impulses to the graphic interface

4. **EFG** $\rightarrow$ graphic interface, which is in a web server

5. **spec** $\rightarrow$ module that is in charge of doing 2D-PSD plots, etc.

The data from various digitizers can be read simultaneously using various servers. Particularly in this work, the two digitizers (CAEN DT5725 and RedPitaya) have their own servers, which are hosted on the same computer together with the HV power supply server on a different machine. The Q_{long}, Q_{short}, pregate, and pretrigger parameters in the server can be changed to access the charge integration of the pulses and to acquire the waveform of each pulse. The CAEN digitizer communicates with the server using the ABCD protocol. The abcdrp module is used for RedPitaya communication. After obtaining the pulse waveform, the waps server provides the pulse charge integration.

3.4   Radioactive sources

The characterization of detectors used a variety of radioactive sources. Gamma-neutron sources were used to optimize the discrimination capabilities, whereas gamma sources were used for energy calibration. The table 3.5 provides detailed information about the sources. The ^{252}Cf gamma-neutron source is used for pulse shape discrimination. Two different types of decay take place in the^{252}Cf nucleus: alpha decay (96.91%) and spontaneous fission (3.09%). Spontaneous fission results in the emission of many neutrons and photons. Fast neutrons with energies around MeV are emitted by the source, and their energy spectrum follows the Maxwellian distribution described by:

$$\frac{dN}{dE} = \sqrt{E}.e^{\frac{E}{t}} \qquad (3.2)$$

For the spontaneous fission of ^{252}Cf, the constant t has a value of 1.3 MeV [1]. The dominant decay mechanism for ^{252}Cf is alpha decay, and the alpha emission rate is about 32 times that for spontaneous fission. The neutron yield is 0.116 n/s per Bq, where the activity is the combined alpha and spontaneous fission rate [1]. The calculated activity of the ^{252}Cf source on the day of experiment (04/04/2022) is 291.78 kBq given the half life of ^{252}Cf is 2.65 years. Then the neutron emission rate is around 33,846. neutrons/sec.

Table 3.5: Information of the radioactive sources used

Source	Activity (kBq)	Date	Emission
^{60}Co	383	01/06/2015	gamma
^{22}Na	384	01/06/2015	gamma
^{137}Cs	386	01/06/2015	gamma
^{252}Cf	2000	03/12/2014	neutron-gamma

3.5   Monte Carlo Simulation

The Monte Carlo Method is a computing approach designed to tackle problems with probability distributions by repeatedly creating random samples. Before revealing the anticipated result, it must perform a significant number of recalculations. Numerous industries, including finance, engineering, supply chain, and science, employ the Monte Carlo simulation extensively. When the system has several degrees of freedom and the standard resolution is not very effective, it is quite practical.

The Monte Carlo method is currently the most effective way for simulating radiation transport through materials. Random steps are used to replicate the particle's history. These steps are interrupted by the particle's interaction with matter, which results in a change in the particle's orientation and a loss of energy. Finally, secondary particles are created. The cross-section predicts the probability of each of these contact mechanisms, so every relevant physical process and every type of particle engaged in the interaction must be accurately modeled in the simulation. For instance, the photoelectric effect, Compton scattering, and pair creation are the main processes of interaction for photons with energy between keV and MeV.

TSystems with complicated geometries and various material media can be easily modelled using the Monte Carlo approach, leading to simulations that closely match the experimental system. In general, identifying the radiation source, the sample that is irradiated, the detecting systems, as well as determining the processes that are involved, under the criteria that the user requires, is necessary for the assembly of the radiation configuration.

For modeling radiation transfer, various simulation programs exist. The most common are FLUKA, MCNPX, GEANT4, PENELOPE, and EGS4. Each code builds a stochastic model based on probability density functions by modeling a random variable's individual events one at a time. From the beginning until the finish, each particle's interactions are tracked [17].

In this study, the experiment that was conducted was simulated using the GEANT4 (version 10.7) code and the Monte Carlo approach. It was carried out with the intention of analyzing the NaIL detector's characteristics. It was possible to provide a more accurate assessment of the geometric efficiency of the detector by matching the energy spectra of the experiment with the simulated spectra. Version 10.7 of GEANT4, a well-known tool that simulates the transport of radiation through matter and is implemented in C++, was utilized in this study. The code includes all elements of the simulation, such as the geometry of the system, the materials used, the fundamental properties, the production of primary particles, the tracking of particles through materials, the physics processes, the response of the detector, the generation of event data, the storage of events and tracks, and a visualization of the detector and particle trajectories. On the basis of the experimental results, all physical and theoretical models are developed [22, 26].

3.5.1   Construction of the simulation

There are numerous steps involved in creating the entire simulation for a desired experimental setup, and they are all described in more detail below:

1. **Detector construction**: The **G4VUserDetectorConstruction class** is where the detector's construction is carried out. Physical volumes and logic are defined here. An element with a composition, a position, and the ability to house many volumes is represented by a logic volume. On the other hand, the physical volume denotes a volume that is contained within the logic volume. The logical volumes are built using G4LogicalVolume, where the material, attributes, and detector sensitivity are defined. The physical volume is then built using G4VPhysicalVolume, where the volume is placed and parameterized. The shapes and sizes are defined using G4VSolid (for example, G4Vbox, G4Tubs). In this work, first a world volume with air was built with a size of 100x100 cm^2, then the NaIL detector was built with a cylinder shape having 50.8 mm of diameter and 50.8 mm of height, around 2" x 2" crystal as it was available in the lab. The NaIL detector was constructed in this work using a cylinder shape with 50.8 mm of diameter and 50.8 mm of height, roughly 2" x 2" crystal as it was accessible in the lab, first creating an air-filled world volume with a dimension of 100x100 cm^2. The density of the detector, 3.66 g/cm^3, and the elemental concentration of Na and I, 49.5 % each, were used to define the composition of the detector. Li was doped with 1 %, with isotropic abundance for ^{6}Li as 95 % and 7Li as 5 %. The detector's provider, Saint Gobain, provides this abundance percentage. It was stated that this volume was a sensitive detector.

2. **General Particle Source**: The primary particles are generated using the **G4VUserPrimaryGeneratorA** class, where a specific class must be called depending on the properties of the primary particles. As an illustration, the G4GeneralParticleSource (GPS) class was utilized for this job, and its setting was handled by a macro. An initial punctual isotropic source was identified, and its location was determined to be 15 cm away from the detector. The simulation included 1 x 10^6 events, with the energies and particle types (neutron or gamma) defined in accordance with the source of interest.
   The solid angle between the detector and source was calculated to direct the events toward the detector's face in order to have better statistics for counts.

3. **Particle Interaction**: The G4UserPhysicsList class described the particles and the interactions, and it implemented two separate libraries: G4EmLivermorePhysics for photon simulation and G4HadronPhysicsQGSP_BIC_HP for neutron simulation. While the G4HadronPhysicsQGSP_BIC_HP library is defined for the neutrons elastic collision, inelastic collision, neutron capture, and fission, the G4EmLivermorePhysics library for gamma contained the photoelectric effect, the Compton scattering, the Rayleigh scattering, and the pair generation.

4. **Event recording**: Additional classes can be utilized to retrieve crucial information. While the G4UserTrackingAction class tracks the particles at a given instant and stores the data, the

G4UserSteppingAction class records the information of the events in each step. These two classes enable access to the energy that each particle deposits in the detector, which may subsequently be used in conjunction with the G4UserEventAction and G4UserRunAction classes to rebuild the energy spectrum.

Chapter 4

Results and Discussion

This chapter is dedicated for the different tests performed in laboratory using the two detectors i.e, NaIL and EJ-309. The experiments conducted for this research were primarily concerned with analyzing how these two detectors responded to neutrons and gamma radiation. In order to distinguish between gamma and neutrons, the study carried out utilizing these two detectors includes calibration, energy resolution, and pulse shape discrimination parameter optimization. Moreover, preliminary studies were performed for EJ-309 coupled with SiPM and tests were done for comparison between the response of EJ-309 coupled with PMT.

4.1 Characterisation of NaIL detector

4.1.1 Energy calibration

For gamma-ray spectroscopy, inorganic scintillators' energy calibration is often based on the detection of a full energy peak (photopeak) following the absorption of gamma-ray quanta in the detector. The energy of the photopeak is therefore employed for the energy calibration.

In order to identify the channel number that corresponds to the peak's center and the region beneath it, the photopeak in the NaIL gamma spectra is the area of interest. The relationship between the peak center's channel number and gamma energy is linear. The number of gammas that were identified, which is dependent on the detection effectiveness, is revealed in the region beneath the photopeak.

In figure 4.1, the calibrated gamma spectrum detected by our NaIL of ^{22}Na source is shown. The ^{22}Na has two photopeaks corresponding to 511 keV and and 1274.54 keV. The photopeaks for the NaIL detector are well described by a Gaussian, or Normal distribution [1].
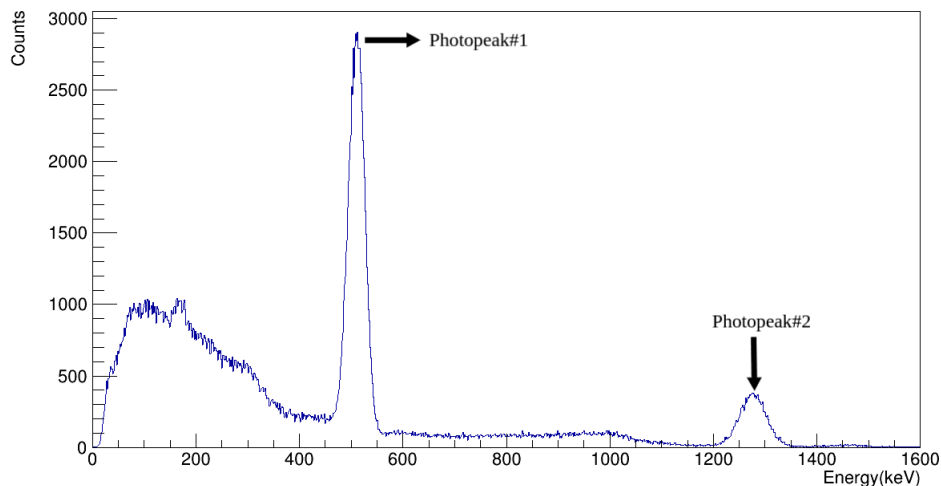

Figure 4.1: Energy calibrated gamma spectra of Na-22 with NaIL.

In order to fit a curve, one assumes that the data follow a particular function that has a number of unknown parameters. The parameters are then changed to find the "best fit". In this study, it is assumed that the photopeaks in the gamma spectra have a Gaussian form. The fit was only made for the data in the vicinity of the photopeak, when these presumptions are true. Three parameters can be used to describe a Gaussian function (h, C_0, and σ):

$$y(Ch) = he$$

where Ch is the channel number, $C_0 h$ is the channel number of the peak center, h is the height of the Gaussian function, and σ is related to the width of the Gaussian shape. The function $y(Ch)$ represents the number of counts in channel Ch using the theoretical fitting function. In this work, the fitting was done using ROOT framework which has an inbuilt function for Gaussian fitting.

The "best fit" to the data is determined by varying these 3 parameters in the fitting function $y(Ch)$ so that $y(Ch)$ replicates the data as close as possible. Mathematically, this is accomplished by defining a chi-square function, χ^2, as follows:

$$\chi^2 = \sum_{Ch=Ch_i}^{Ch=Ch_f} \left(\frac{y(Ch) - Exp(Ch)}{\sqrt{Exp(Ch)}} \right)^2 \tag{4.2}$$

where $Exp(Ch)$ is the experimental value for the number of counts in channel Ch. The statistical uncertainty of $Exp(Ch)$ is $\sqrt{Exp(Ch)}$. The chi-square function is just the sum of the sum of the squares of the difference between the fitting function, y(Ch), and the data divided by the error from an initial channel Ch_i to a final channel Ch_f. The smaller the value of the χ^2 function, the better the curve y(Ch) fitting the data.

The "best-fit" is determined by finding values for these 3 parameters which make χ^2 as small as possible. This technique is called chi-square minimization, and is used in many areas of data analysis. As discussed above, the channel number of the photopeak is approximately proportional to the energy of the gamma (or X-ray) particle. In this work, a linear relationship has been assumed between channel number and energy:

$$E = aCh + c \tag{4.3}$$

where E is the energy of the gamma and Ch is the channel number of the center of the photopeak. The constant a is a scaling factor with units of energy/(channel number) and c is the intercept with units of energy. To determine the scaling factor a and intercept c, a known gamma source like Cs-137 was taken. Then by measuring the channel number of this gamma, the constant a and c can be determined. Once a and c is known, the energy of an "unknown" gamma can be determined from the channel number of the photopeak, Ch, and the equation above 4.3.

In practice, it is better to use more than one standard source for the energy calibration of the detector. Hence, in the calibration of NaIL, three gamma sources ^{137}Cs, ^{60}Co and ^{22}Na were used. It is important to note that ^{22}Na and ^{60}Co have two gamma photopeaks, so the channel numbers of 5 gamma particles of known energy were measured. Then a "best-fit" line, through these data points, is used as a calibration line as shown in figure 4.2
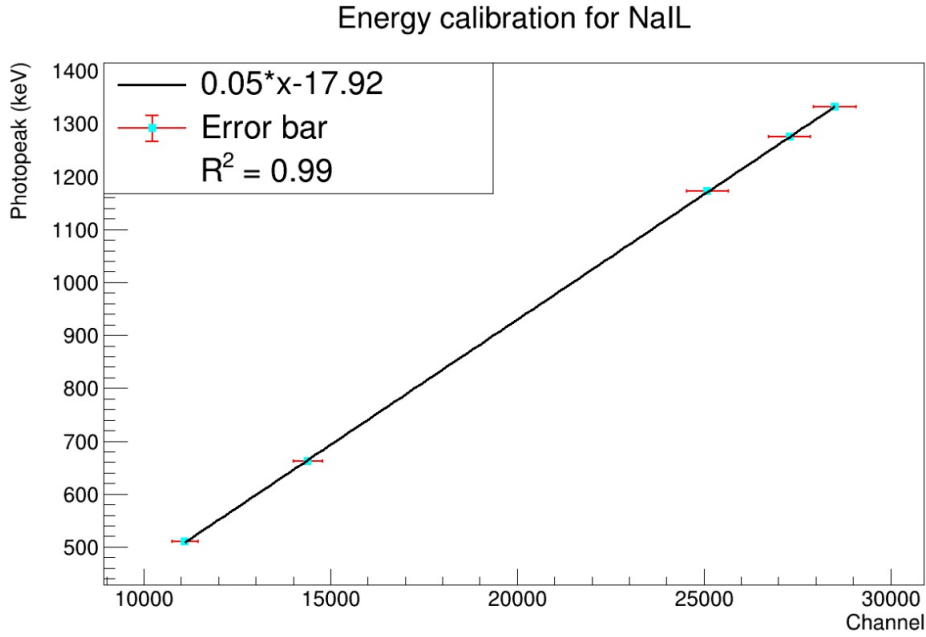
Figure 4.2: Gamma energy calibration of the NaIL 2"x2" with DT5725 digitizer.

It can be seen from the calibration plot that the fit agrees very well with the data and has a R^2 of 0.99. [1]

4.1.2   Energy resolution

Energy resolution calibration and efficiency calibration both need to be done accurately for a scintillator to show promise in performance. Any detector's energy resolution is measured by its capacity to tell apart two peaks. This feature is dependent on the FWHM number, which stands for Full Width at Half Maximum. The detector's ability to discriminate two gamma rays with similar energy flowing from the source to the detector [32] increases with decreasing FWHM value. The FWHM, or full width at half maximum, is the width of the photopeak. FWHM is given by,

$$\text{FWHM} = 2 * \sqrt{\ln 2} \frac{\sigma}{C_0} \tag{4.4}$$

where σ is the standard deviation of the fitted Gaussian distribution and C_0 is the channel number of the center of the photopeak. Then the resolution, R is defined:

$$R = \frac{\text{FWHM}}{E_0} \tag{4.5}$$

where E_0 is the photopeak.
Figure 4.3 shows the resolution vs energy plot for NaIL. A resolution of 6.5% at 662 keV is determined which is typical for NaI scintillators [37]. The fit applied in the resolution plot is expressed by a power law ($x*E^y$) which is inspired from the work [45].

---

[1]R^2 is used to quantify the amount of variability in the data that is explained by defined model. It's useful for comparing the fits of different models.
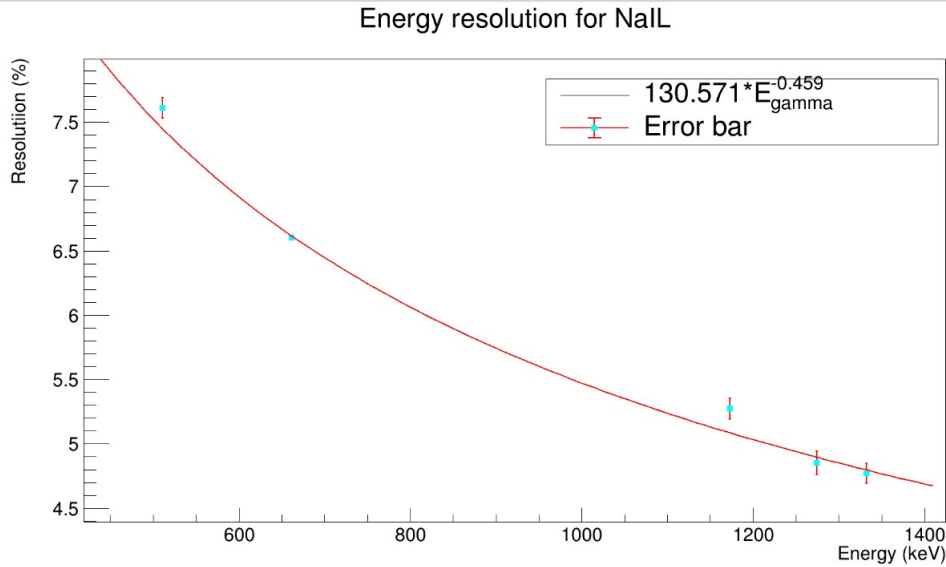
Figure 4.3: NaIL Energy resolution plot.

4.1.3 Optimization of thermal neutron / gamma discrimination

Optimizing the parameters of the digitizers was important to obtain the best response and maximize the neutron/gamma discrimination capabilities of the NaIL detector. The technique used to distinguish between neutrons and gamma photons is known as Pulse Shape Discrimination (PSD) 4.2.2. The Q_{short} and Q_{long} are time windows for charge integration which need to be optimal (equation 4.6). In figure 4.4, the integration windows are shown.
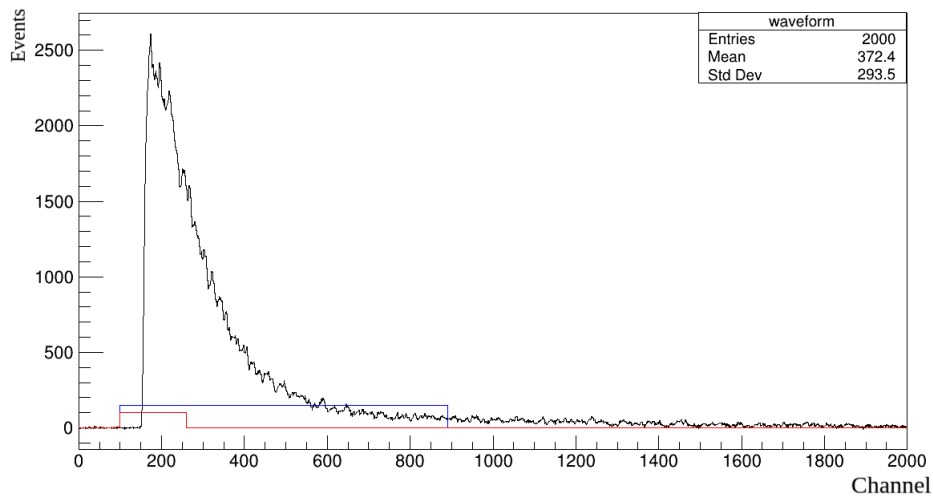
Figure 4.4: Q_{long} (blue) and Q_{short} (red) integration windows for DT5725 digitizer.

$$\text{PSD} = \frac{Q_{long} - Q_{short}}{Q_{long}} \tag{4.6}$$

In order to obtain the mentioned objective, a neutron-gamma source of ^{252}Cf was used. The polyethylene and lead blocks of thickness 6 cm and 25 cm respectively were used to slow down the neutrons from ^{252}Cf which can then be detected by the NaIL. The measurement with ^{252}Cf was carried out for around 30 minutes in order to have a good count. During the measurement the digitized waveforms were recorded, each waveform with an acquisition window of around 4 ns. The pregate and pretrigger

were set at 50 ns and 150 ns respectively.

The offline analysis was performed to optimize the integration windows consisted of choosing events with energies between 3280 and 3760 keVee from the energy spectrum, as illustrated in figure 4.5. As shown in figure 4.6., the events in this energy range are plotted as a function of PSD, and the FoM is then calculated by performing two Gaussian fits of the neutrons and gamma events. Then, the optimization is found for the highest value of the FoM by keeping Q_{long} constant and changing the value of Q_{short}. Once the value of Q_{short} at which the best FoM is obtained, then that Q_{short} value is kept constant and the process is repeated while adjusting the value of the Q_{long}. The optimized value of the FoM for NaIL was found to be 4.10 ± 0.02 which is in good agreement with the published results [4]. The respective values of Q_{long} and Q_{short} for the corresponding FoM are 790 ns and 160 ns. This value of FoM shows that NaIL detector have excellent gamma/neutron discrimination capability.
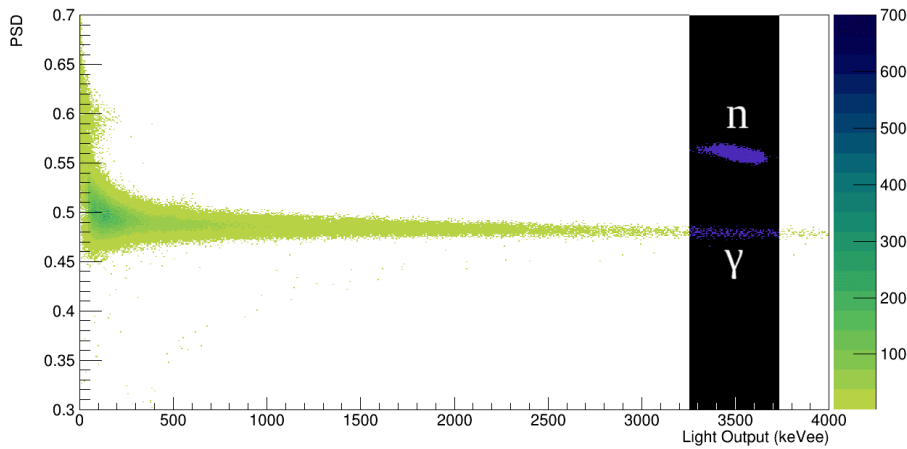
Figure 4.5: Pulse shape discrimination (PSD) parameter versus energy for ^{252}Cf source. Fast neutrons were slowed down by polyethylene and lead blocks with a total thickness of 31 cm. The black strip indicates the energy region used for PSD optimization. For the energy calibration we used gamma sources, therefore keVee (kilo electron Volt electron equivalent) as the unit of measurement of energy is used. The best value for FoM obtained is **4.10±0.02**.
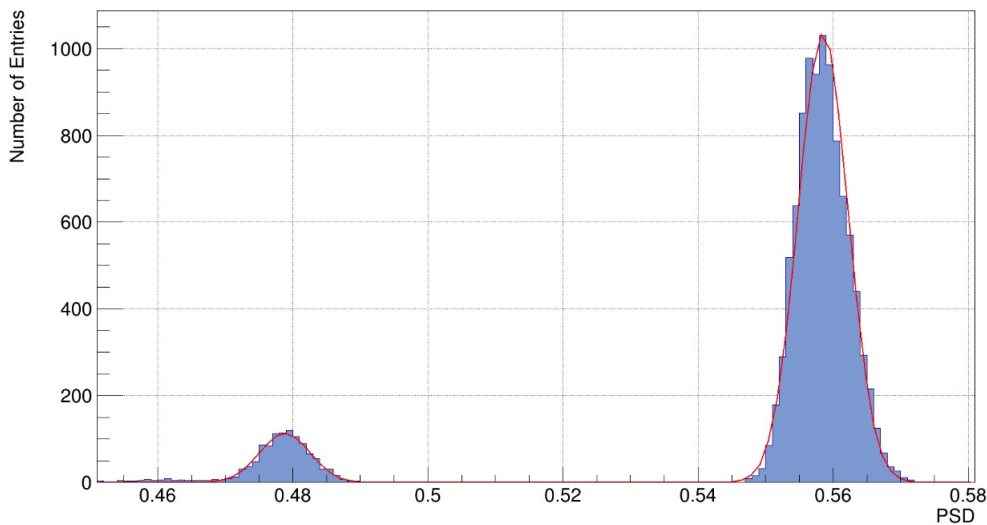
Figure 4.6: Gaussian fit for the gamma (left) and the neutron (right) to calculate the FoM for NaIL coupled to SiPM. Corresponding FoM = 4.10.

In tables 5.2 and 5.3 below, the FoM calculated for different integration windows along with the

uncertainty are reported. As discussed before, first the Q_{short} integration window is changed while keeping Q_{long} constant at 650 ns, the best FoM is obtained at $Q_{short} = 160$ ns. Then in the next step, Q_{short} is kept constant at 160 ns and Q_{long} is varied until the best FoM = **4.10 ± 0.02** is obtained at $Q_{long} = 790$ ns.

Q_{long} (ns)	Q_{short} (ns)	FoM	Δ FoM
650	75	1.33	0.01
650	80	2.12	0.02
650	100	2.80	0.02
650	110	3.13	0.02
650	120	3.30	0.02
650	130	3.38	0.02
650	140	3.50	0.02
650	150	3.53	0.02
650	**160**	**3.60**	**0.02**
650	170	3.55	0.02
650	180	3.50	0.02
650	190	3.50	0.02
650	200	3.45	0.02

Table 4.1: FoM and uncertainty in FoM for different values of Q_{short} at a constant value of $Q_{long} = 650$ ns

Q_{short} (ns)	Q_{long} (ns)	FoM	Δ FoM
160	600	3.44	0.02
160	700	3.58	0.02
160	750	3.65	0.02
160	**790**	**4.10**	**0.02**
160	800	3.74	0.02
160	850	3.68	0.02

Table 4.2: FoM and uncertainty in FoM for different values of Q_{long} at a constant value of $Q_{short} = 160$ ns

The uncertainty in the FoM was determined by using the error propagation formula discussed in the Appendix 7.2.

4.1.4 Full-Energy Peak Efficiency

Full-Energy Peak Efficiency is defined as the ratio of counts in the full energy peak (photopeak) corresponding to energy E ($N_P(E)$), to the number of photons with energy E emitted by the source ($F(E)$)

$$\varepsilon_P(E) = \frac{N_P(E)}{F(E)} \tag{4.7}$$

$\varepsilon_P(E)$ depends on the source-detector geometry and on the energy. Figure 4.7 represents the full-energy peak efficiency vs energy of gamma. The experimental values represent the gamma-sources used, ^{137}Cs, ^{22}Na and ^{60}Co. Geant4 simulations were also performed for different energies for comparison.
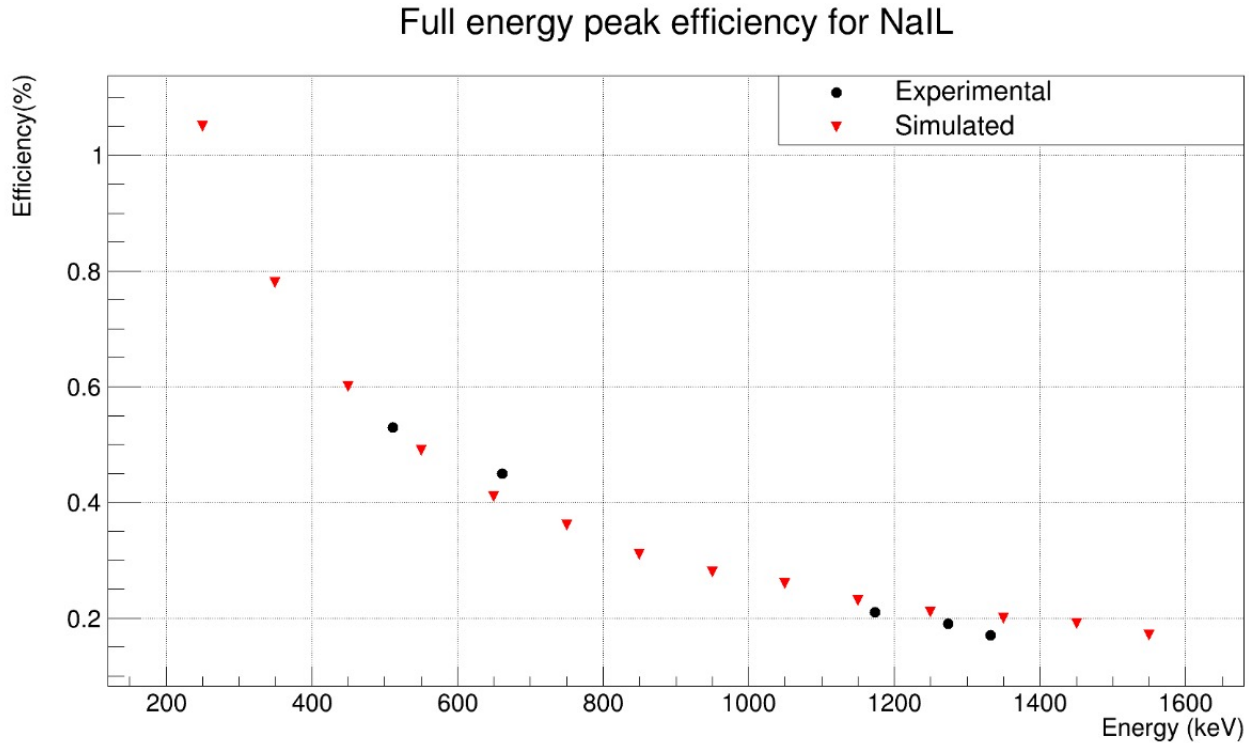
Figure 4.7: Full energy peak efficiency for different gamma sources. The black circles represent the experimental values while the red inverted triangles represent the simulated values using Geant4.

As can be seen from the plot, the efficiency decreases the energy of the gamma increases. This trend is similar for both experiment and simulation. Moreover, the experimental values closely agree to the simulated values.

4.1.5   Moderation of neutrons from ^{252}Cf

Once the characterization of NaIL was done, it was ready to be used for tests in the scope of CLE-ANDEM project. The first simple test consisted of counting the neutrons from ^{252}Cf after passing through different materials like Polyethylene, Teflon and Graphite placed covering the detector crystal. The selection of material and thickness is important for the moderation of neutrons. Therefore, the neutron counts were studied as a function of different thickness of materials.

Measurement

The optimal parameters obtained for NaIL were used for the measurement using CAEN DT5725 digitizer. First, the measurement was taken without any material covering the NaIL as a control. The measurement was taken for 10 minutes in order to have a good count. The first material to be used was graphite. We started with a block of graphite having thickness 2 cm, afterwards graphite of thickness 6 cm, 10 cm and 14 cm was kept by adding more blocks. The source ^{252}Cf was kept at a distance of 15 cm from the detector and was kept constant in each case. The acquisition time was also kept constant which was 10 minutes.

The next material that was used was polyethylene. The same order of thickness was used as for the graphite with the same source having same distance from the detector and also the acquisition time. The third and last material to be used was Teflon. Since, we were using blocks of materials having certain thickness, the teflon blocks had a different thickness than graphite and polyethylene. Therefore, the order of thickness used for teflon was 3.1 cm, 7.3 cm, 11.5 cm and 16 cm. The measurement time and distance between the source and the detector were kept constant.

Analysis

The analysis was performed on ROOT. Since, the neutrons and gammas are recorded simultaneously on a 2D PSD plot. The neutron spectrum needed to be segregated from the gamma spectrum. This was only possible thanks to the excellent discrimination capabilities of NaIL. A feature of the ROOT known as TCut was used in order to separate the neutron spectrum. TCut allows to select a particular section of the plot which can be analysed separately. As an example, figure 4.8 shows the neutron section being cut from the 2D PSD plot of neutrons and gamma of ^{252}Cf using graphite of thickness 2 cm.
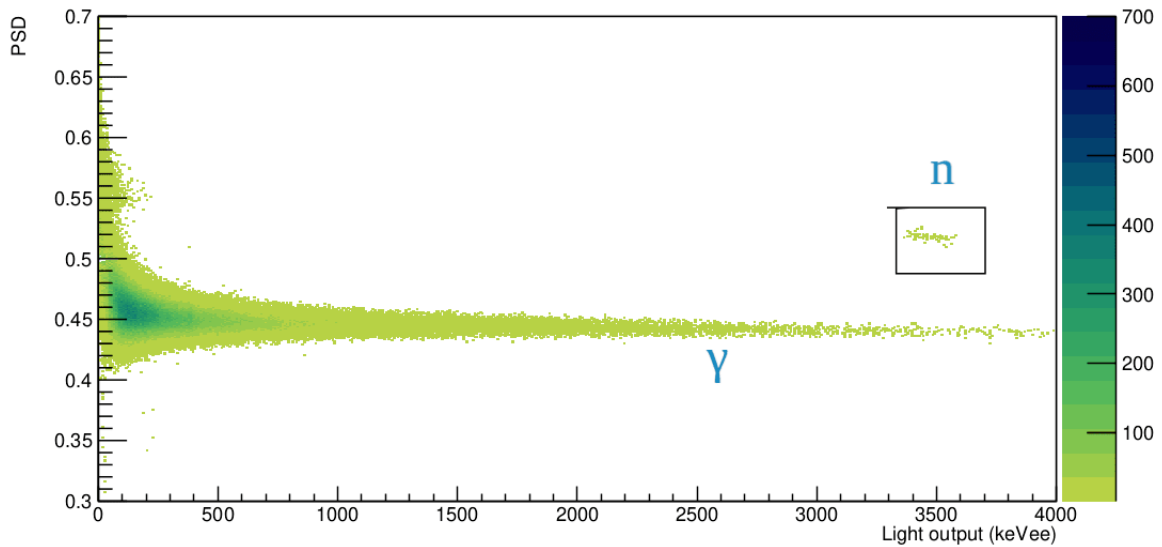
Figure 4.8: The black box represents the TCut selection of neutrons in a 2D PSD plot. The material covering the NaIL is graphite with a thickness of 2 cm.

Once the selection is done, the counts can simply be obtained on ROOT using Integral function. The neutron counts were normalised with time in each case as the acquisition time was not exactly kept constant.

Results

The table 4.3 shows the normalised neutron counts with increasing thickness. It can be seen that the neutron count decreases with the increase in thickness.

Graphite Thickness (cm)	Neutron counts/sec
2 ±0.1	0.49 ±0.03
6 ±0.1	0.44 ±0.03
10 ±0.1	0.41 ±0.03
14±0.1	0.42 ±0.03

Table 4.3: Normalised neutron counts for each thickness of graphite.

Similarly, table 4.4 represents the neutron counts per second with the increase in thickness of polyethylene. The important observation is the rapid increase in neutron counts for thickness 6 cm, then again the neutron counts decreases with the increase in thickness.

Polyethylene Thickness (cm)	Neutron counts/sec
2 ±0.1	1.30 ±0.05
6 ±0.1	3.09 ±0.07
10 ±0.1	2.42 ±0.06
14±0.1	1.62 ±0.05

Table 4.4: Normalised neutron counts for each thickness of polyethylene.

The last material to be studied was Teflon. Table 4.5 shows the different thickness of teflon used to cover the NaIL and neutron counts per second.

Teflon Thickness (cm)	Neutron counts/sec
3.1 ±0.1	0.45 ±0.03
7.3 ±0.1	0.58 ±0.03
11.5 ±0.1	0.46 ±0.03
16 ±0.1	0.64 ±0.03

Table 4.5: Normalised neutron counts for each thickness of teflon.

It can be seen that the neutron counts first increases with the increase in thickness, then decreases and once again rapidly increases.

Discussion

Neutrons are completely undetectable to a detector of comparable size because they can pass through many centimeters of stuff without any sort of contact. When a neutron interacts, it does so with the absorber material's nucleus. The neutron may completely vanish and be replaced by one or more secondary radiations as a result of the contact, or else its energy or direction may be drastically altered. The secondary radiations produced by neutron interactions are usually invariably heavy charged particles, unlike gamma rays. These particles could be either nuclear processes caused by neutrons or they could be the nuclei of the absorbent material itself that have been given energy by neutron collisions [1].

The strong force that exists between nuclei and neutrons is the primary way that they interact. Due to the small range of this force, these reactions are significantly more uncommon than those involving single neutrons and protons. Since normal matter is mostly empty space, neutrons must approach the nucleus at a distance of around 10^{-13} cm before they interact. As a result, the neutron is a very penetrating particle [2].

When the neutron does interact, it may undergo a variety of nuclear processes depending upon its energy:

1. Elastic scattering: A(n,n)A

2. Inelastic scattering: A(n,n')A

3. Radiative neutron capture: n+(Z,A) $\rightarrow$ γ +(Z,A+1)

4. Fission

5. High energy hadron shower production

It is significant to remember that these interactions are energy-dependent. According to [42], in our situation, ^{252}Cf has a Maxwellian energy distribution that spans from 0.5 to 13 MeV. The different materials used in order to thermalisew the neutrons are Graphite (C) having density 2.26 g/cm^3,

teflon $(C_2F_4)_n$ with mass density $2.2 \, g/cm^3$ and polyethylene $(C_2H_4)_n$ with mass density $0.857 \, g/cm^3$. These materials slow down the incoming neutron from the ^{252}Cf source. The slowing down of fast neutrons is known as moderation.

Upon using different materials in combination of different thickness, it can be concluded that the lighter the nucleus (material), the more recoil energy it absorbs from the neutron. This implies of course that the slowing down of neutrons is most efficient when protons or light nuclei are used. Therefore, if we look upon the chemical formula of materials used, teflon having C_2F_4 nuclei slows down the incoming neutrons the least, Graphite which has only Carbon nuclei follows teflon while polyethylene, C_2H_4 having Carbon and twice the Hydrogen than carbon acts as the best moderator, therefore polyethylene with a thickness of 6 cm acts as the best moderator resulting the thermalised neutrons to interact with ^{6}Li in the NaIL detector by the reaction ^{6}**Li(n,t)**α. Hence, giving rise to the highest neutron counts in the detector. Figure 4.9 shows the neutron counts per second versus thickness of different materials used for comparison. It can be concluded that in high radiation zones where there are neutrons present with a velocity distribution, NaIL can be used as a counter by using polyethylene with a thickness of 6 cm as a shielding material.
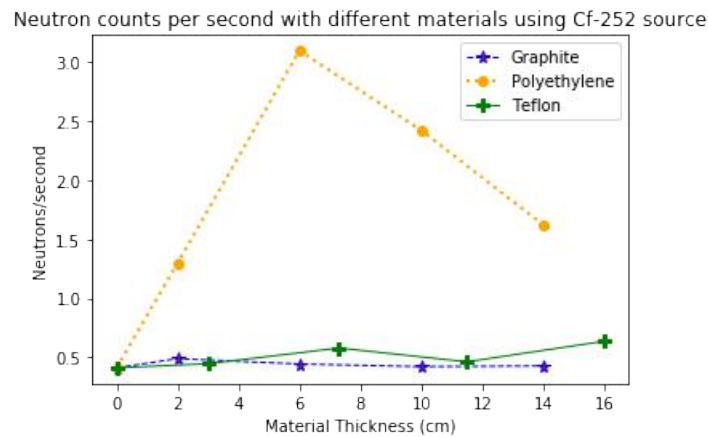
Figure 4.9: Neutron counts per second versus thickness of material. Polyethylene has the highest neutron rate due to the presence of large amount of hydrogen which acts as a good moderator.

4.2 Preliminary studies: EJ-309 coupled to a SiPM array

A portable and small fast neutron detection system can be created by combining a SiPM matrix and a liquid scintillator (with PSD capabilities). Because of this, a study was conducted in this work employing SiPM matrices and an organic liquid scintillator, EJ-309, in order to replace the PMT with SiPM and compare and select the best combination for a detection system. If the detecting system is surrounded by a strong magnetic field, this method will offer a small and lightweight setup, as well as reduced power consumption and increased stability.

In this subsection, we start with the same steps as we discussed in the section above i.e, first calibration and then optimizing short and long gates in order to determine the optimal FoM.

4.2.1 Energy Calibration

There is no photopeak that relates the channel to the gamma-ray energy since the response of the gamma-rays in organic scintillators depends on the Compton distribution obtained by the recoil electrons. As a result, the Compton edge's energy is employed for the energy calibration. Equation 4.8 is

used to determine each gamma-Compton ray's edge..

$$(E_e)_{max} = \frac{2E_\gamma{}^2}{2E_\gamma + m_ec^2} \tag{4.8}$$

where $(E_e)_{max}$ is the maximum energy transferred to the electron, E_γ is the energy of the incoming photon, and m_e is the mass of the electron. In order to calibrate the detector, the Compton edge energy of each gamma-ray was assigned to the channel where the amplitude of the Compton plateau reaches 80% of its maximum intensity [27]. Figure 4.10 represents the spectrum of ^{22}Na of the 2"x2" EJ-309 detector coupled to a 4x4 NUV SiPM using CAEN digitizer DT5725. Two Compton edges of the ^{22}Na are seen in the uncalibrated spectrum (counts vs. channel), and the two calibration points are indicated.
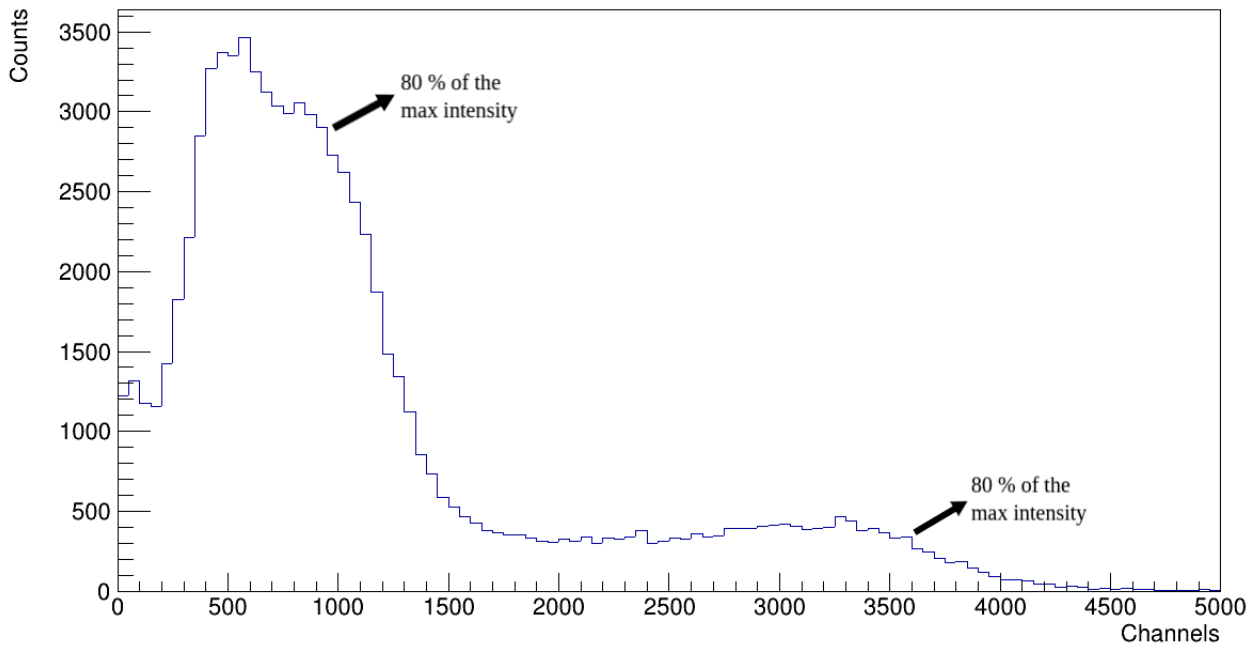
Figure 4.10: Gamma energy spectrum of the ^{22}Na without the energy calibration, using the EJ-309 coupled to SiPM

Figure 4.11 shows the calibration curve of EJ-309 with SiPM. The different gamma sources used were ^{137}Cs, ^{60}Co and ^{22}Na. The two Compton edges of ^{60}Co cannot be seen due to limitation in the resolution of the EJ-309 scintillator. Therefore for calibration purpose, the average energy of the two Compton edges was taken.
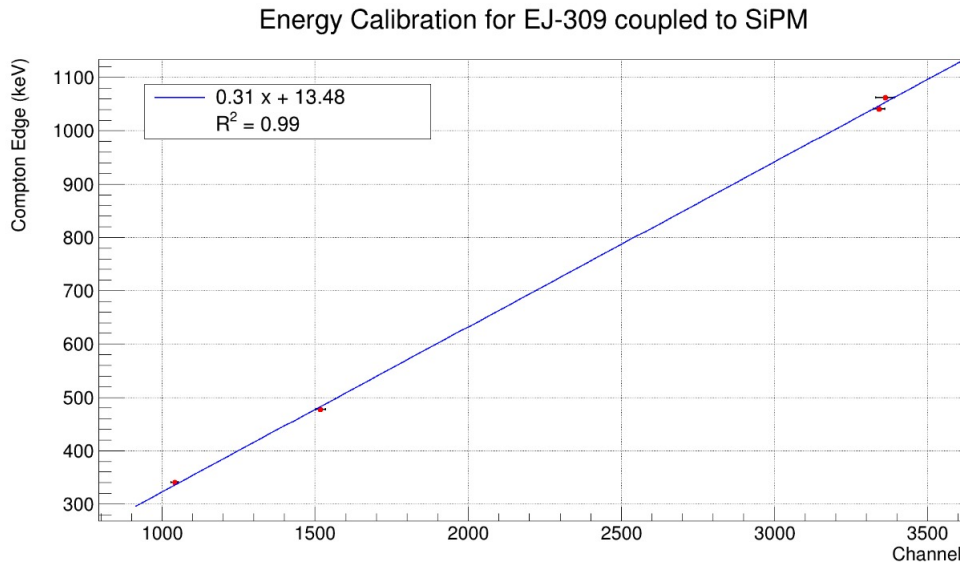
Figure 4.11: Gamma energy calibration of the 2"x2" EJ-309 cell coupled to SiPM with DT5725 digitizer using gamma sources ^{137}Cs, ^{22}Na and ^{60}Co.

4.2.2 Optimization of fast neutron and gamma discrimination

Once the calibration is done, the neutron/gamma discrimination capabilities of the EJ-309 detector needs to be maximized. For this, it was necessary to optimize the parameters of the digitizers in order to get the best response as discussed in subsection 4.2.2. For this objective a neutron-gamma source of ^{252}Cf was used with CAEN DT5725 digitizer. The measurement with neutron-gamma source ^{252}Cf was carried out for around 32 minutes to have better counts. During the measurement the digitized waveforms were recorded, each waveform with an acquisition window of around 4 ns.

The optimization of the integration windows consisted in doing an offline analysis similar to the one explained in subsection . The the energy spectrum of all the events that have energy between 900 keVee and 1400 keVee were selected as shown in figure 4.12. This selection corresponds to the Compton edge associated with the gamma-ray energy of 1274.537 keV (^{22}Na).

Figure 4.12: Pulse shape discrimination parameter versus energy for ^{252}Cf source for EJ-309 coupled with SiPM. The black strip indicates the energy region used for PSD optimization. For the energy calibration we used gamma sources, therefore keVee (kilo electron Volt electron equivalent) as the unit of measurement of energy is used.

The events in this energy range are plotted as a function of PSD then the FoM is computed by doing two Gaussian fittings of the neutrons and gamma events as shown in figure 4.13. The pregate and

the pretrigger for the measurement were set at 15 ns and 150 ns respectively. The optimized value of the FoM for EJ-309 coupled with SiPM found to be 1.36 ± 0.03. The respective values of Q_{long} and Q_{short} for the corresponding FoM are 350 ns and 70 ns.
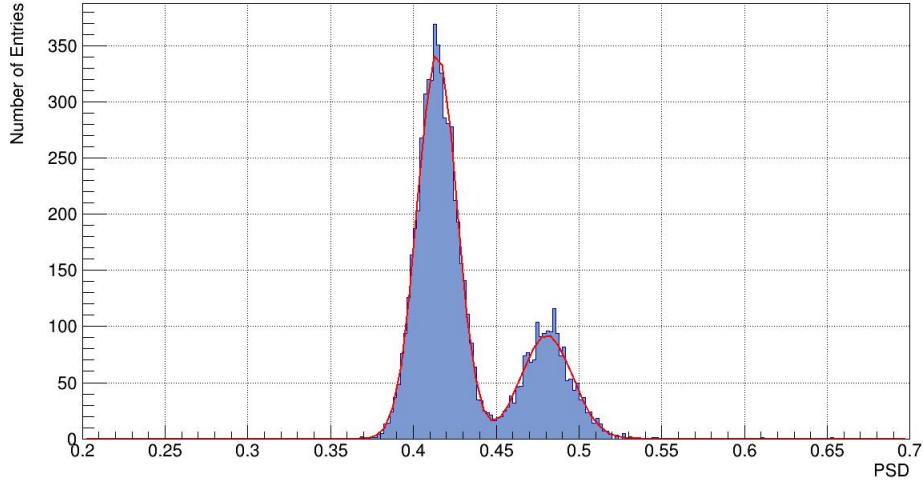
Figure 4.13: Gaussian fit for the gamma (left) and the neutron (right) to calculate the FoM for EJ-309 coupled to SiPM. Corresponding FoM = 1.36.

4.2.3   EJ-309 coupled to PMT

For the comparative study of EJ-309 coupled with SiPM, the calibration and gamma/fast neutron discrimination optimization was also performed for EJ-309 coupled with PMT. In this section, the PSD plot and FoM values are presented for comparison with the SiPM assembly of EJ-309. The tests and analysis performed as for EJ-309 coupled with PMT are discussed in more detail in the appendix section 7.3. In the end, the FoM values and qualitative comparison for resolution for both the combination of the detection system is discussed.

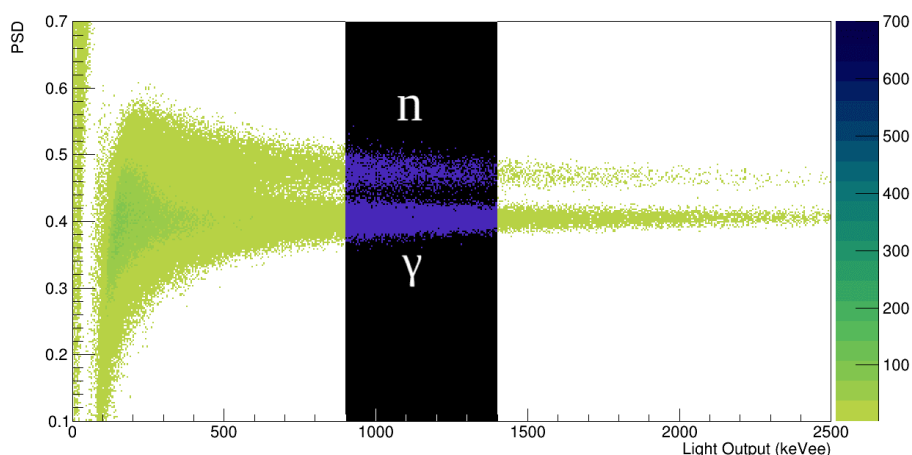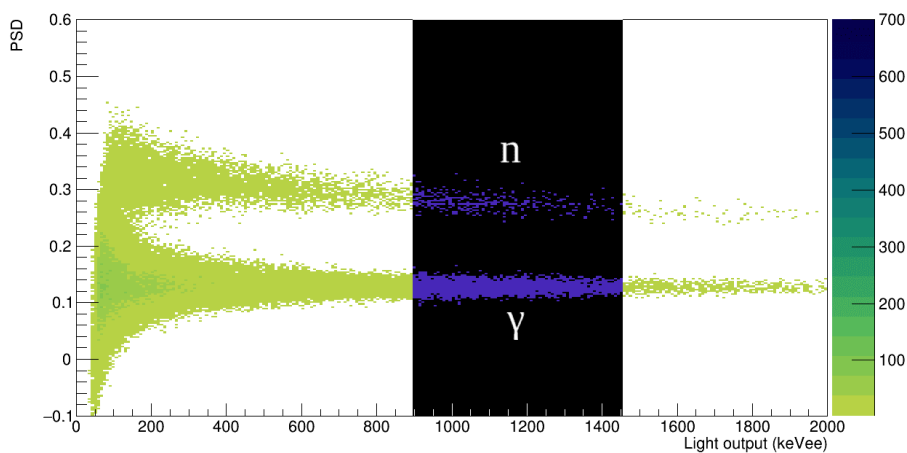Figure 4.14: Pulse shape discrimination parameter versus energy for ^{252}Cf source for EJ-309 coupled with PMT. The black strip indicates the energy region used for PSD optimization. For the energy calibration we used gamma sources, therefore keVee (kilo electron Volt electron equivalent) as the unit of measurement of energy is used.
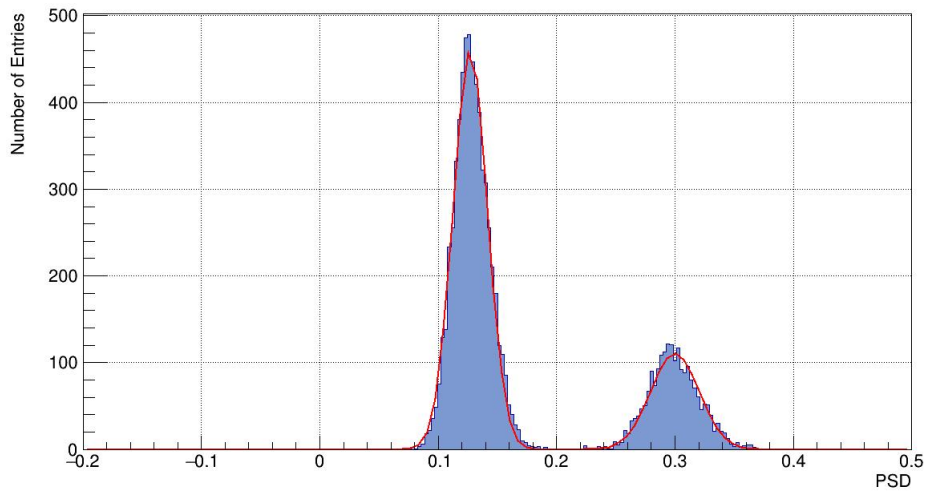
Figure 4.15: Gaussian fit for the gamma (left) and the neutron (right) to calculate the FoM for EJ-309 coupled to PMT. Corresponding FoM = 2.34.

4.2.4   Resolution: SiPM vs PMT

A qualitative comparison for the resolution of two assemblies of EJ-309 (SiPM and PMT) was performed. This comprised of plotting the spectra of the different gamma sources ^{137}Cs, ^{22}Na and ^{60}Co obtained from EJ-309 coupled to SiPM and EJ-309 coupled to PMT. Then, a linear fit was performed from the peak of the Compton edge to its tail for both the calibrated spectrum obtained from SiPM (red) and PMT (blue). The value of the slope, m provides a comparison for the resolution as the longer tail after the Compton edge implies a lower resolution while a shorter or compact tail after the Compton edge means the detector assembly has better resolution.

The different comparison plots from ^{137}Cs, ^{22}Na and ^{60}Co are shown in figures 4.16, 4.17 and 4.18 respectively.
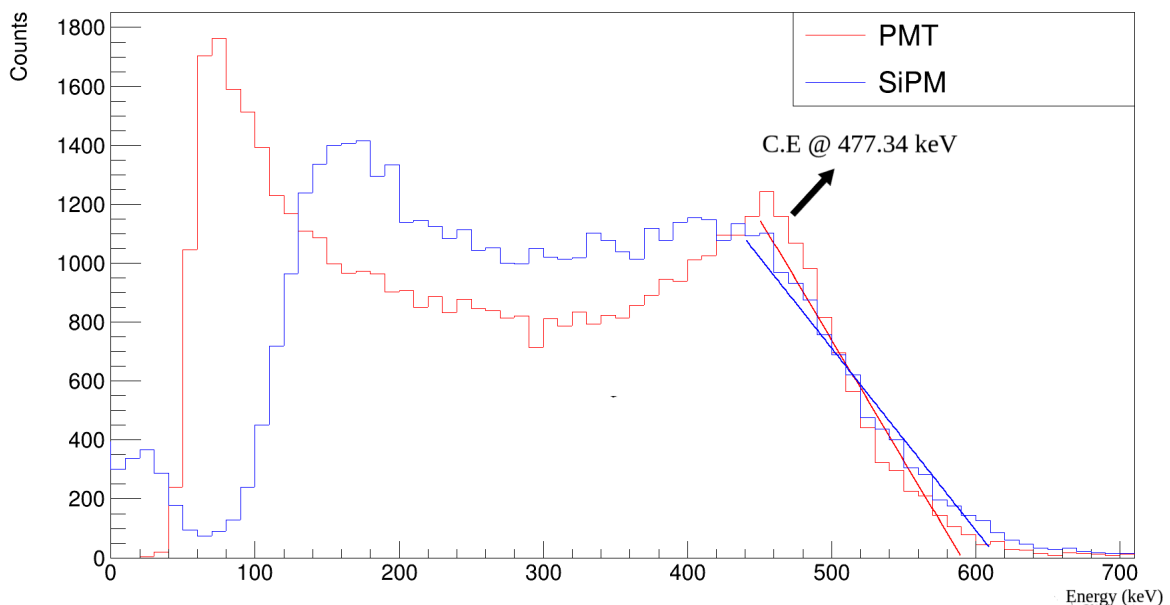
Figure 4.16: Calibrated gamma spectrum of ^{137}Cs with the EJ-309 coupled to SiPM (blue) and EJ-309 coupled to PMT (red). The fit is performed at the start of the Compton edge to its tail. The longer tail implies lower resolution and therefore smaller value of slope.

The fit performed from the Compton edge to the tail for PMT has a slope of -8.2 while the slope for SiPM has a value of -6.18. The slope has a higher value in the case of PMT. It can also be seen that

the Compton edge tail for PMT is shorter than SiPM and therefore the EJ-309 assembly with PMT has better resolution.
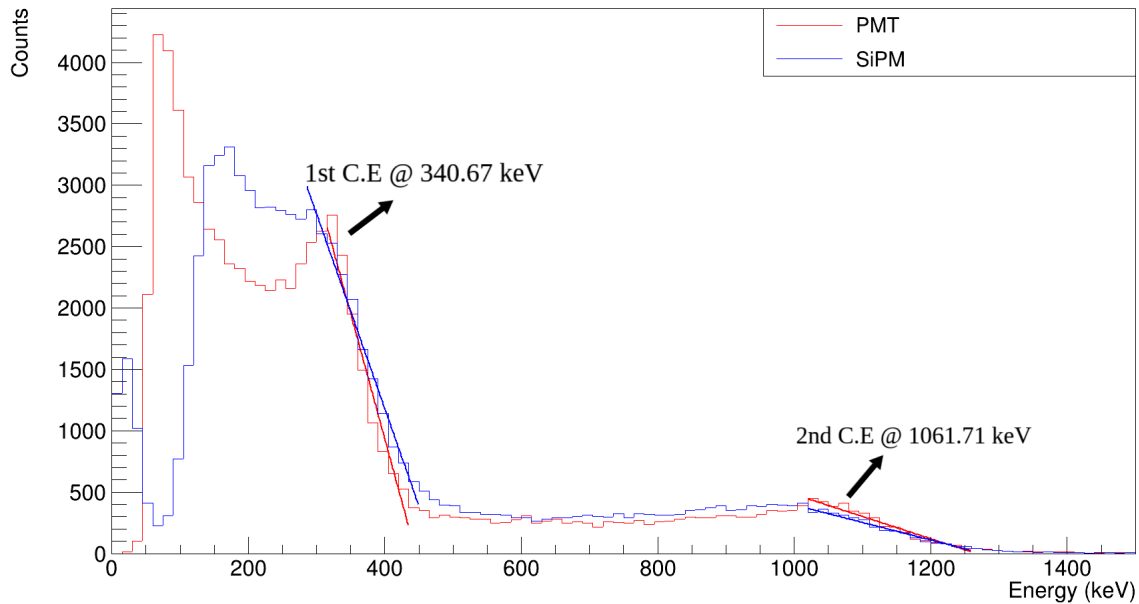
Figure 4.17: Calibrated gamma spectrum of ^{22}Na with the EJ-309 coupled to SiPM (blue) and EJ-309 coupled to PMT (red). The two Compton edges (CE) corresponding to photopeak energy 511 keV and 1274.54 keV are represented in the plot. The fit is performed at the start of the Compton edge to its tail. The longer tail implies lower resolution and therefore smaller value of slope.
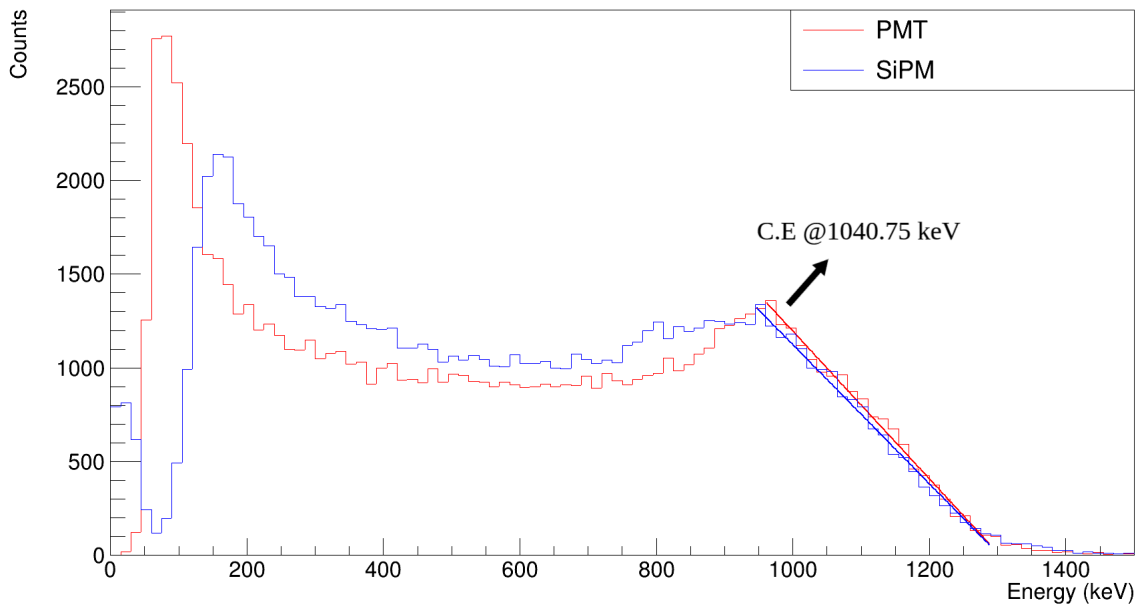
Figure 4.18: Calibrated gamma spectrum of ^{60}Co with the EJ-309 coupled to SiPM (blue) and EJ-309 coupled to PMT (red). ^{60}Co has two Compton edges (CE) but due to the limited resolution of the detector, the two Compton edges are not distinguished. Therefore, the average energy (1040.75 keV) of the two Compton edges is taken for calibration. The fit is performed at the start of the Compton edge to its tail. The longer tail implies lower resolution and therefore smaller value of slope.

Similarly, in the case of ^{22}Na, the slope for the fit in case of PMT has values (-20.40 for 1st Compton edge and -1.80 for 2nd Compton edge) which is bigger than the slope values obtained for SiPM (-15.86 for 1st Compton edge and -1.43 for 2nd Compton edge).

For ^{60}Co, the resolution of the EJ-309 detector is not good enough to distinguish two Compton edges corresponding to 963.39 keV and 1118.11 keV, the average energy of both the Compton edges is used for calibration. The slope value for the Compton edge fit in this case for the PMT is -3.94 and for SiPM -3.72.

The prime reason for lower resolution of the SiPM assembly compared to PMT assembly of EJ-309 is due to the loss of scintillation light in case of SiPM assembly. The EJ-309 cell as shown in figure 3.2 has a circular shape while the 4x4 SiPM assembly shown in 3.4 is square is shape and does not completely overlap the EJ-309 cell. This leads to the leakage of the scintillation light. On the other hand, the H1941 PMT as shown in figure 3.3 completely covers the cell avoiding any leakage of the scintillation light. Therefore, this difference in the geometry results in poor resolution of the EJ-309 coupled with SiPM compared to EJ-309 coupled with PMT.

4.2.5   Conclusion

The comparative study between the EJ-309 coupled to the SiPM and EJ-309 coupled to the PMT shows the assembly of the EJ-309 with PMT has better resolution along with better gamma/neutron discrimination capability. Table 4.6 shows the FoM values for both the assemblies along with the slope values for the fit performed for Compton edge obtained from ^{137}Cs, ^{22}Na and ^{60}Co.

	EJ-309 SiPM	EJ-309 PMT
Slope: ^{137}Cs	-6.18	-8.20
Slope: ^{22}Na	-15.86, -1.43	-20.40, -1.80
Slope: ^{60}Co	-3.72	-3.94
FoM	1.36	2.34

Table 4.6: Table representing the comparative factors for different detection assembly employed for EJ-309.

Although, the SiPM assembly with EJ-309 is promising in terms of compactness, lower power consumption and faster detector response. However, due to the difference in geometrical shape and size of the EJ-309 cell and SiPM, there is a leakage of the scintillation light which results in poor resolution of the detection system. Therefore, for the further tests EJ-309 coupled to the PMT is a better candidate.

Chapter 5

Laboratory tests for radiological survey

After the characterization of the inorganic scintillator NaIL and having performed preliminary studies of the EJ-309 scintillator, further tests were performed addressing the major objectives of this thesis work. A prototype of the Unmanned Ground Vehicle (UGV) was assembled which can carry the detection system and can be set in motion. The first objective was to determine the location of the radiation hotspot and the later one being the identification of the radionuclide contributing to the radiation hotspot. This chapter discusses the assembly of the mobile detection system, the tests performed, their analysis and the results.

5.1 Hotspot localization with Unmanned Ground Vehicle (UGV)

Since the original Unmanned Ground Vehicle (UGV) for CLEANDEM project is still under development, we improvised a prototype to test the detector which is shown in figure 5.1.
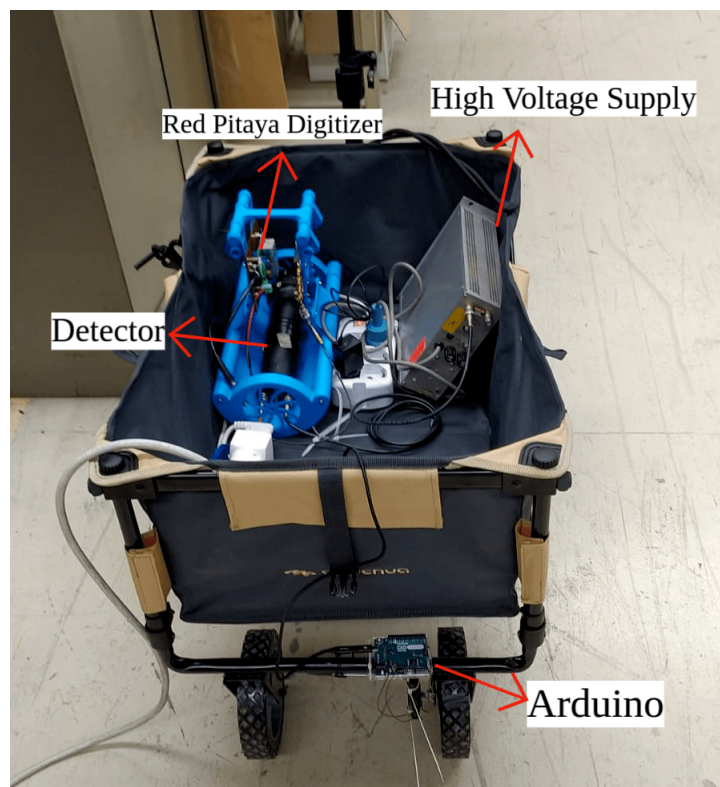
Figure 5.1: Different components of the UGV prototype.

The UGV consisted of different components mentioned below:

1. A movable cart which can hold the weight of detector assembly and electronics.

2. Detector assembly with red-pitaya digitizer. A clear image of red-pitaya digitizer is shown in figure 3.9.

3. A mobile high voltage supply having positive polarity for NaIL.

4. An Arduino installed at the base of the rover (cart) next to the wheel to calculate the speed of the UGV.

The objective of the UGV prototype was to determine the gamma/neutron hotspots and radionuclide identification using the NaIL detector in motion. To demonstrate the working of the assembled detection system, a gamma source was used to detect the incoming photons. The source was kept stationary while the cart was in motion. The function of the Arduino was to determine the speed at which the cart moves. It does so by registering each rotation of the wheel and the time at which one complete rotation is completed. Then, the distance covered by the UGV can be calculated given the radius of the wheel. By calculating the time difference between beginning of the motion of cart and its end, the average speed can be determined easily.

5.1.1 Experimental Setup

The assembly of the UGV prototype was discussed in the section 5.1. The hotspot distance consisted a straight path of 20 metres marked by a tape so that the UGV is moved along a straight line. The straight distance was chosen for the sake of simplicity and to check the working of different components of the UGV. The gamma source ^{137}Cs was kept at the position which is middle point of the 20 metres distance and at a perpendicular distance of 1 metre from the hotspot line. The 1 metre distance was chosen in order to have an appreciable number of counts as well as not being very close to the hotspot point. Figure 5.2 shows the scheme of experimental setup developed for hotspot localization.
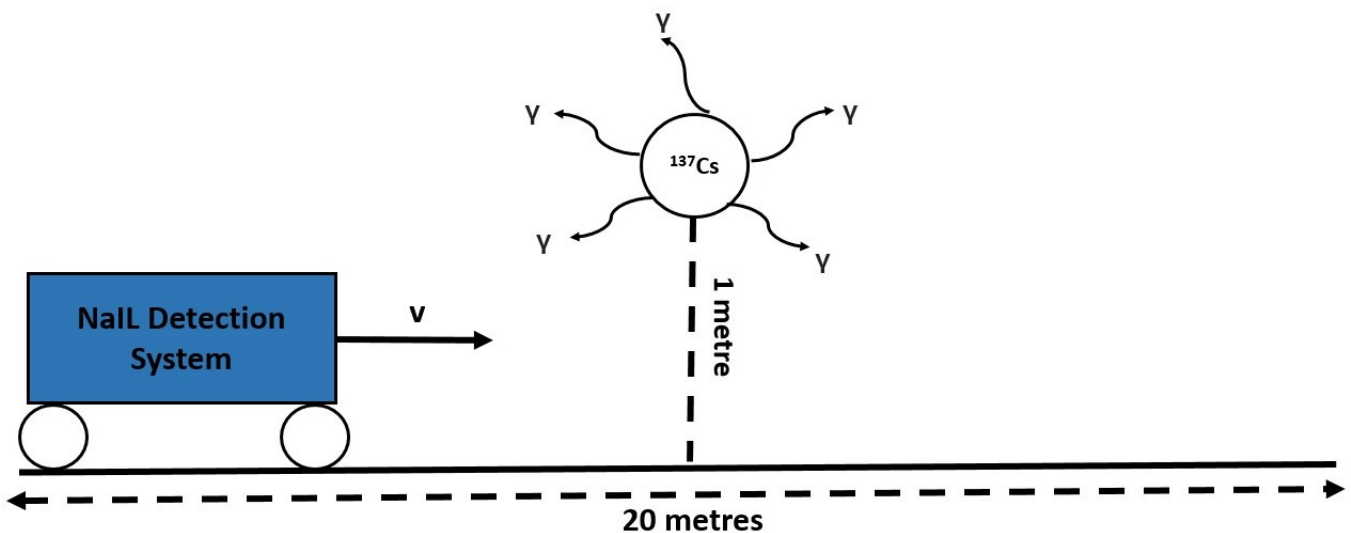
Figure 5.2: Illustration of the experimental setup for hotspot localization. The ^{137}Cs source was placed at a perpendicular distance of 1 metre from the middle point of 20 metres distance. The ^{137}Cs source is emitting gammas isotropically.

As the UGV was made to move manually like a trolly, the time duration was recorded for each run in order to calculate the speed and the test was performed at each different speeds of the UGV prototype.

5.2   Gamma hotspot localization

As mentioned earlier, one of the key objectives of the CLEANDEM project is the remote localization of the gamma/neutron hotspots. In order to do so, the UGV prototype was assembled and the NaIL detector was used for gamma hotspot localization. The gamma source ^{137}Cs was fixed at a point and the UGV prototype was manually set in motion. The speed of the UGV prototype was kept close to being uniform as it was set in motion manually. The test was done with different speeds in order to check the optimal speed of the UGV for the detection of hotspot. This speed is dependent on the detector response and the digitizer. The Red-Pitaya digitizer was used as it is light weight, portable along with appreciable ADC resolution of 14 bits and sample rate of 125 MS/s.

5.2.1   Analysis

The analysis consisted of synchronizing two files: the first file which records the time and gamma counts every 5 seconds from the digitizer while the other file recording the space and time from the Arduino .
The two files needed to be synchronized first before going on for further analysis. The synchronization basically consisted of obtaining the counts registered in one file to the distance recorded in the other file.
For the synchronization, a code was written on Python. The time difference between the two files was first calculated, then this time difference was then added to the file lagging in time to make a common reference. One important point to notice here is that the counts were noted every 5 seconds while the the other file registering the space did not have exactly a uniform time interval difference as the time was recorded for every rotation.
As mentioned earlier, the speed of the UGV was very close to being uniform and it was confirmed from the file which recorded time for each rotation completed. The relationship between the time and space recorded by the Arduino was linear. Moreover, the digitizer was recording the gamma counts every 5 seconds. Therefore, the distance at every 5 seconds when the gamma counts were registered was interpolated from the linear relationship of space and time. Once we have the values for the every point in space when the counts were taken, the distance versus the gamma counts were plotted for every file.

5.2.2   Results

Having performed the analysis for each test, the results are plotted as gamma counts versus distance. Ideally, the plot should be symmetrical i.e, the counts should be minimum at both the ends and maximum at the center. Depending on the speed of the UGV, the maximum counts peak in the plot is supposed to shift as the digitizer sampling rate is the same. The speed of the UGV prototype was increased as we performed more measurements. Figure 5.3 shows the plot of the first test with the lowest speed of the UGV prototype.
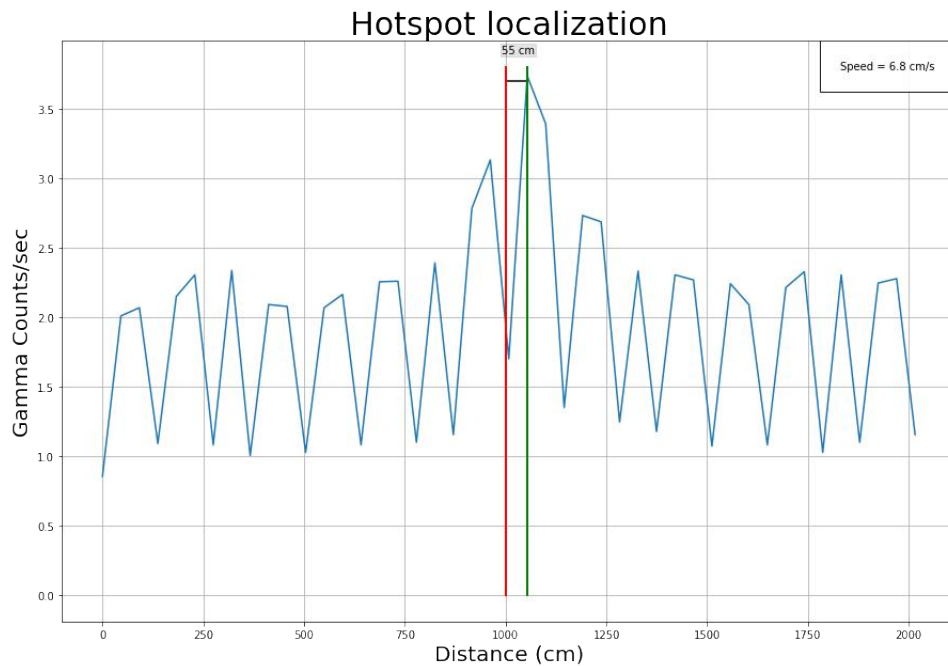
Figure 5.3: Gamma counts per second plot versus distance. The average speed of the UGV is 6.8 cm/s.

The red line parallel to y axis represents the 10 meter distance at which the ^{137}Cs source was placed while the green line represents the actual hotspot location. It can be seen that the maximum counts are found at a distance at 1055 cm (10.55 m). The shift should be taken into account during the analysis procedure. The average speed of the UGV was 6.8 cm/s.

After that, few other tests were done using the same configuration but by increasing the speed of the UGV in order to study the gamma counts as a function of speed. Moreover, it was also interesting to study the shift in the location of the radiation hotspot as the speed of the UGV increased. The results are shown in figures 5.4 and 5.5.
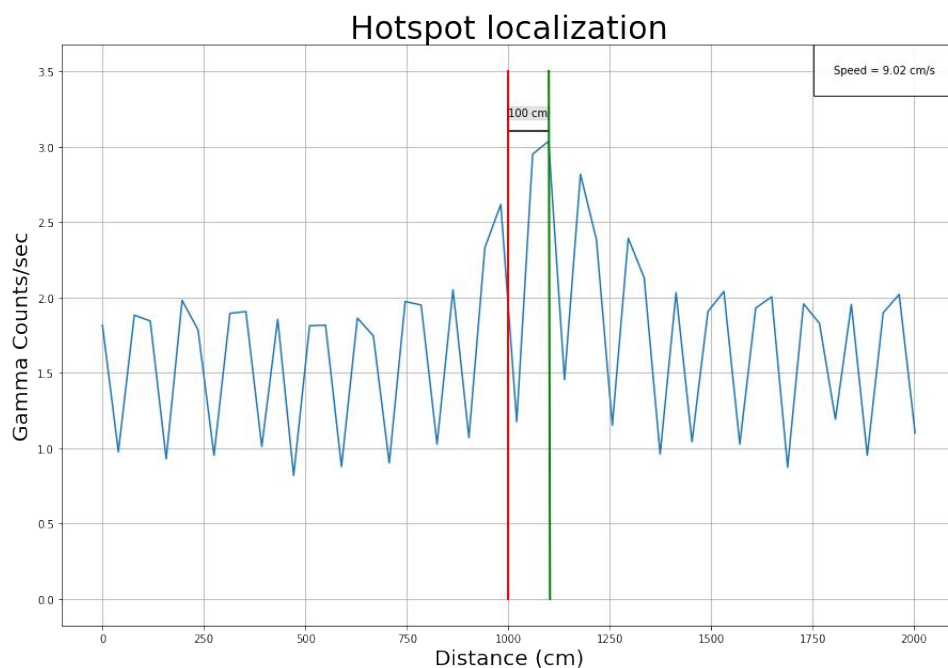
Figure 5.4: Gamma rate plot versus distance. The average speed of the UGV is 9.02 cm/s.
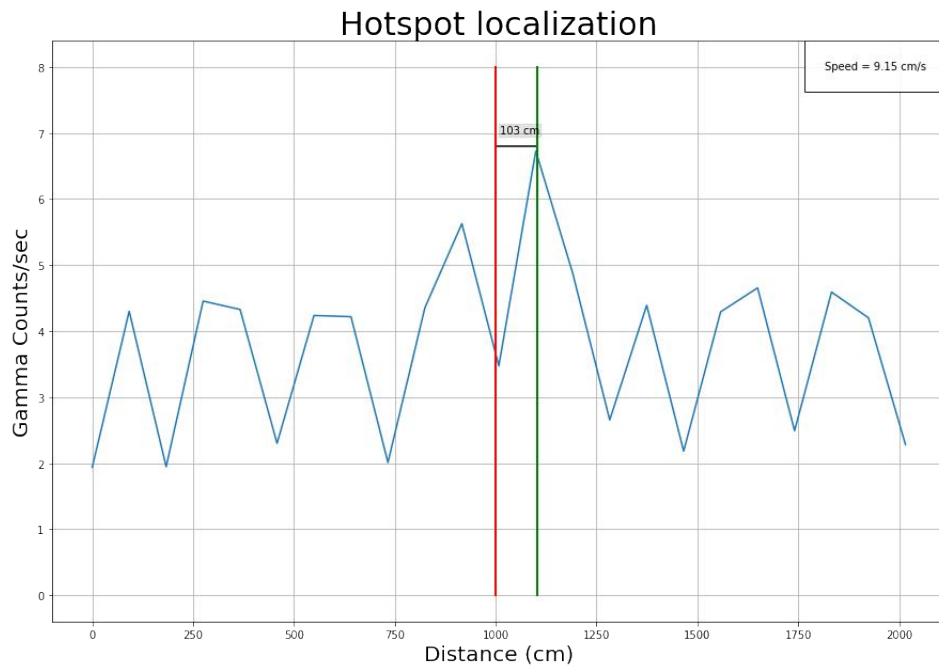
Figure 5.5: Gamma rate plot versus distance. The average speed of the UGV is 9.15 cm/s.

It can be clearly be seen from figures 5.4 and 5.5 that the maximum counts are shifted to the right as compared to fig. 5.3. This shift can be explained due to the increase in the speed of the UGV. Another important observation is that since the speed of the UGV in both these cases is similar, the shift is almost negligible.

Having performed tests at lower speeds, further measurements were performed at higher speeds in order to study its effect on the detection system.

Figures 5.6 and 5.7 represent the gamma counts versus distance plots at speeds of 10.48 cm/s and 13.42 cm/s.
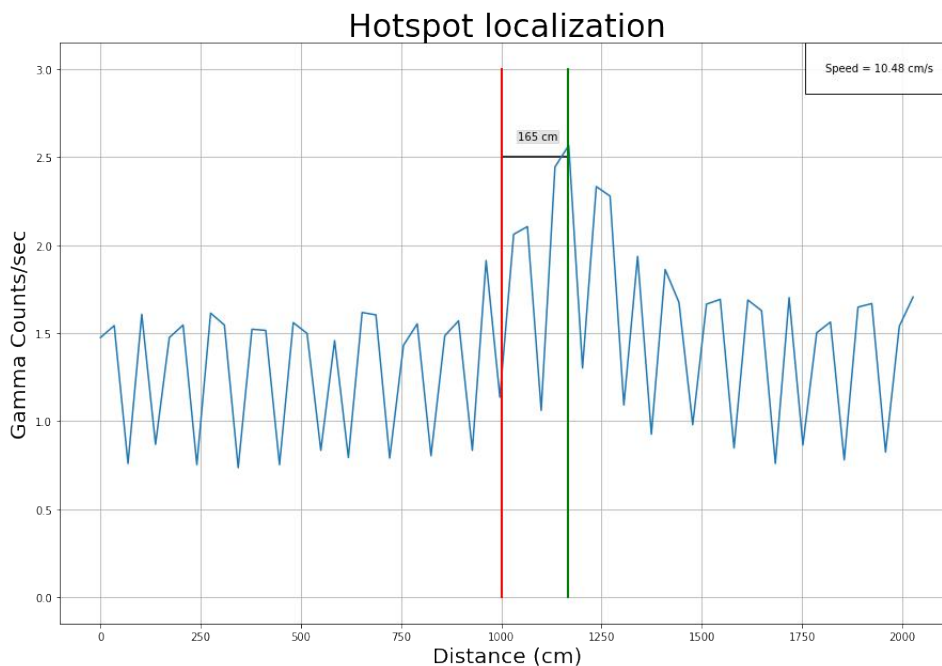
Figure 5.6: Gamma rate plot versus distance. The average speed of the UGV is 10.48 cm/s.
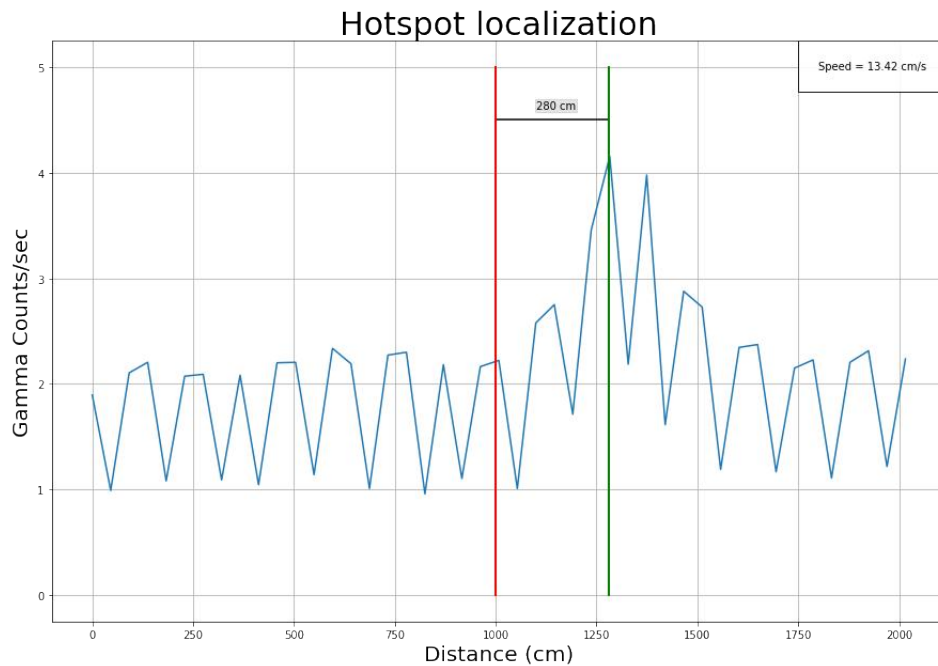
Figure 5.7: Gamma rate plot versus distance. The average speed of the UGV is 13.42 cm/s.

Once again, the shift in the hotspot location is shown to be increased with the increase in the speed. Another measurement was performed with an average speed of 23.5 cm/s in order to study the behaviour of the shift with respect to the speed. The result is shown in figure 5.8.
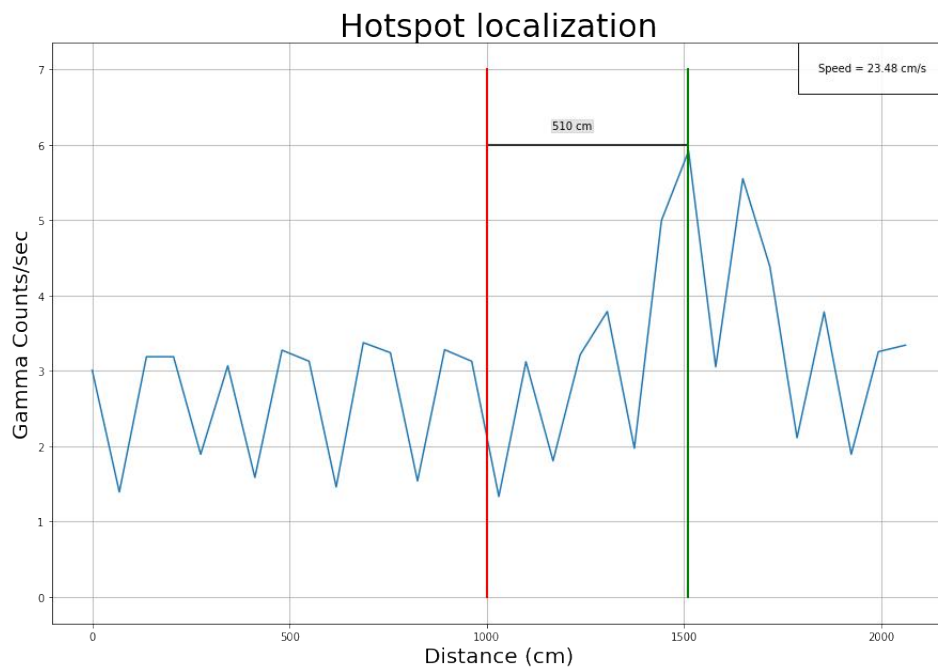
Figure 5.8: Gamma rate plot versus distance. The average speed of the UGV is 23.48 cm/s. The actual position of the hotspot is found to be around 1510 cm (15.1 m) which is 5 metres away from the actual location.

As can be seen the increase in the speed of the UGV does not go in the favor of the gamma hotspot localization. The counts are supposed to be maximum at the center as the source is closest and therefore the counts should be maximum. The maximum counts peak is shifted towards the right of the actual hotspot location. There is a trend observed in the shift of the hotspot location as the speed increased

from 6.8 cm/s to 23.5 cm/s. There exists a condition for the accuracy in the hotspot localization: at lower speeds of the UGV prototype, the hotspot can be very well located. As the speed increases, the shift in the hotspot location starts to increase. Therefore, we have to compensate the accuracy in the hotspot location by decreasing the speed of the UGV prototype.

5.2.3   Discussions

Table 5.1 summarizes the different speeds of the UGV prototype at which hotspot localization tests were performed with the shift in the hotspot location from the actual location.

Table 5.1: Table representing the shift in the hotspot location from the actual position with the increase in the speed of the UGV prototype.

Speed (cm/s)	Hotspot location (cm)	Shift in hotspot (cm)
6.8	1055	55
9.02	1100	100
9.15	1103	103
10.48	1165	165
13.42	1280	280
23.48	1510	510

From table 5.1, it can be seen that with speed 10 cm/s or lower, the hotspot location accuracy is well within 2 metres. Therefore, the optimal speed for point source hotspot location detection can be said 10 cm/s. With lower speeds, this accuracy can be improved. After performing the measurements with UGV equipped with NaIL and using Red-pitaya digitizer at different speeds, the optimal speed range was determined. The gamma counts were recorded as a function of distance. The optimal speed range given the linear geometry was found out to be 7 cm/s to 9 cm/s. Indeed, if the speed of the UGV is slower, the plot will get better. But in order to increase the efficiency of D&D operations and reduce the detection time of the UGV to locate the hotspot, an optimal speed range is needed.

With speeds higher than the optimal one, the hotspot was shifted from the center reducing the accuracy. The shift is always towards the right side of the actual position of the hotspot which should be taken into account during the analysis procedure. The optimal speed range for the UGV is from 7 cm/s to 10 cm/s. Above this range, the analysis should take into account a correction of the position of the hotspot due to the speed.

Once the measurements were performed for the gamma source ^{137}Cs, similar measurement was also performed for gamma-neutron source ^{252}Cf. However, the available ^{252}Cf source was not strong enough that the detector placed at a perpendicular distance of 1 metre from it, could detect any neutrons. Therefore, another more active source was needed to perform the measurements and study the neutron/gamma discrimination capability of the NaIL while being mounted on the UGV.

5.3   Radionuclide identification

Once the hotspot is localized, the next job of the detector is to determine the different radionuclides comprising the hotspot. For this purpose, the detector should have a certain resolution in order to differentiate the different gamma peaks emitting from a number of radionuclides. First a measurement was performed to determine the background radiation. The next measurements were performed to locate and identify the radiation hotspot and radionuclide respectively comprising of ^{137}Cs .

In order to identify the ^{137}Cs from background radiation, a histogram was recorded with intervals of 10 seconds. The histogram file recorded the time, bin width and gammas received by the detector.

5.3.1 Analysis & Results

The first step consisted of testing the detection system which included recording the gamma spectrum of ^{137}Cs. Since we used only one gamma source, the calibration of the detector was not possible but the recorded spectrum shows the channel number at which the gamma photopeak is recorded which can be used as a reference for further measurements.

Figure 5.9 shows the gamma spectrum of ^{137}Cs when the UGV prototype was stationary.
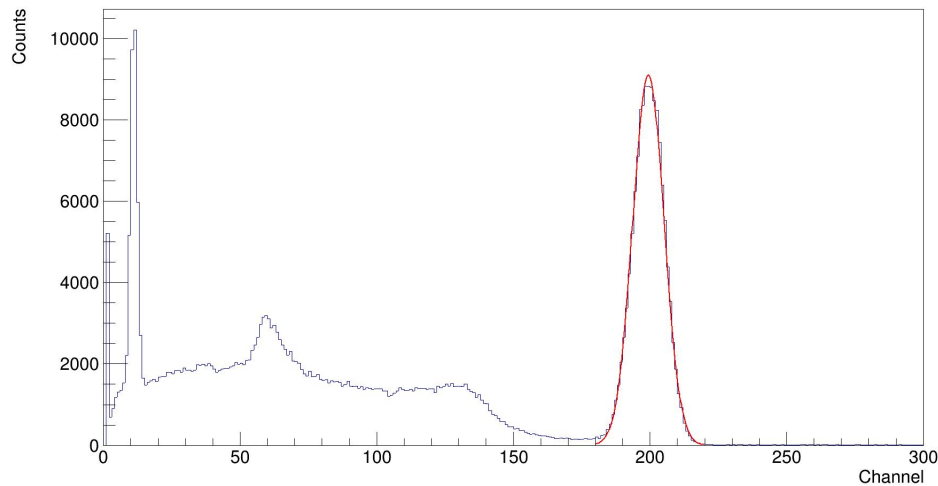
Figure 5.9: Gamma spectrum of ^{137}Cs recorded when the UGV was at stationary. The photopeak (red) which is Gaussian in shape is present symmetrically around channel number 200.

The above gamma spectrum which was used to for calibration also confirms that the detection system is working well. The photopeak is present around channel number 200. Figure 5.10 represents the ^{137}Cs gamma spectrum after calibration.
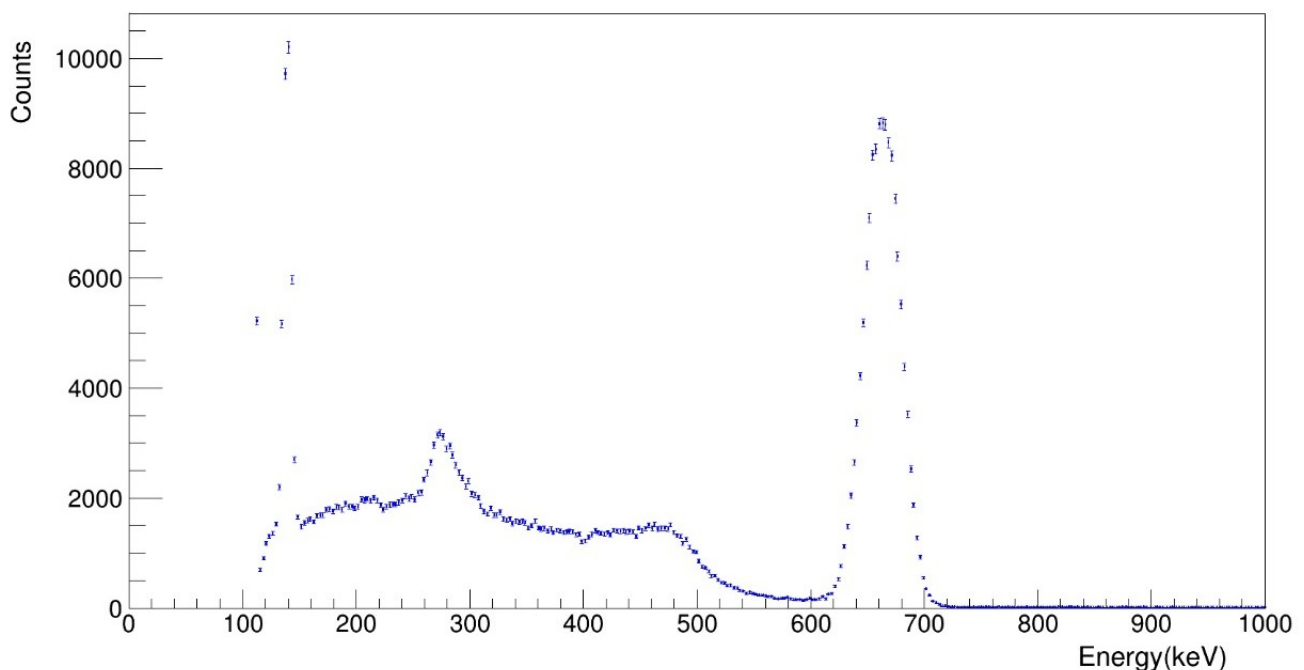
Figure 5.10: ^{137}Cs gamma spectrum after calibration.

The next step consisted of doing background measurement while the UGV is set in motion. Figure 5.11 shows the background radiation in the absence of ^{137}Cs gamma source.
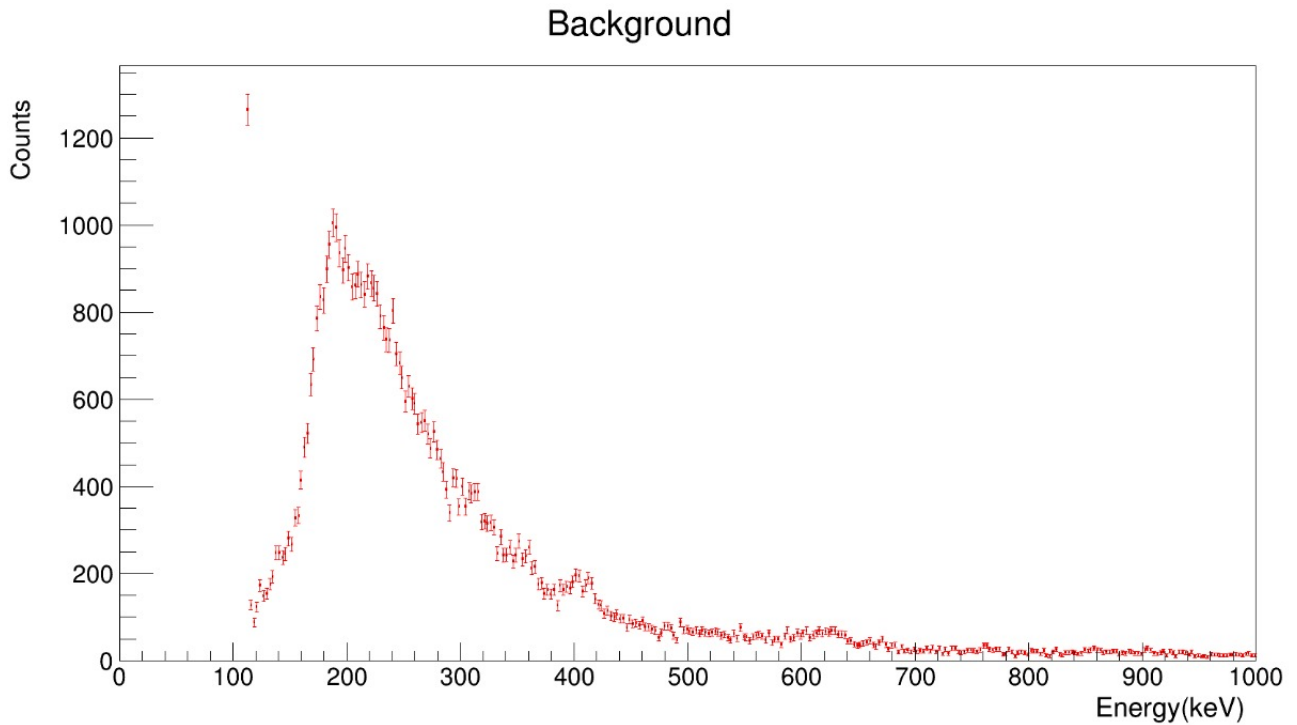
Figure 5.11: Background radiation measurement in the absence of ^{137}Cs while the UGV prototype is in motion.

Having taken the reference for radioisotope identification and background measurement, the final step was to take the measurements with the ^{137}Cs which comprised of the hotspot. Once, the measurement was performed for hotspot localization and its identification, the background was then subtracted and the specific photopeak energy of ^{137}Cs was observed at 661.6 keV.

Figure 5.12 shows the gamma spectrum with the background suppressed.
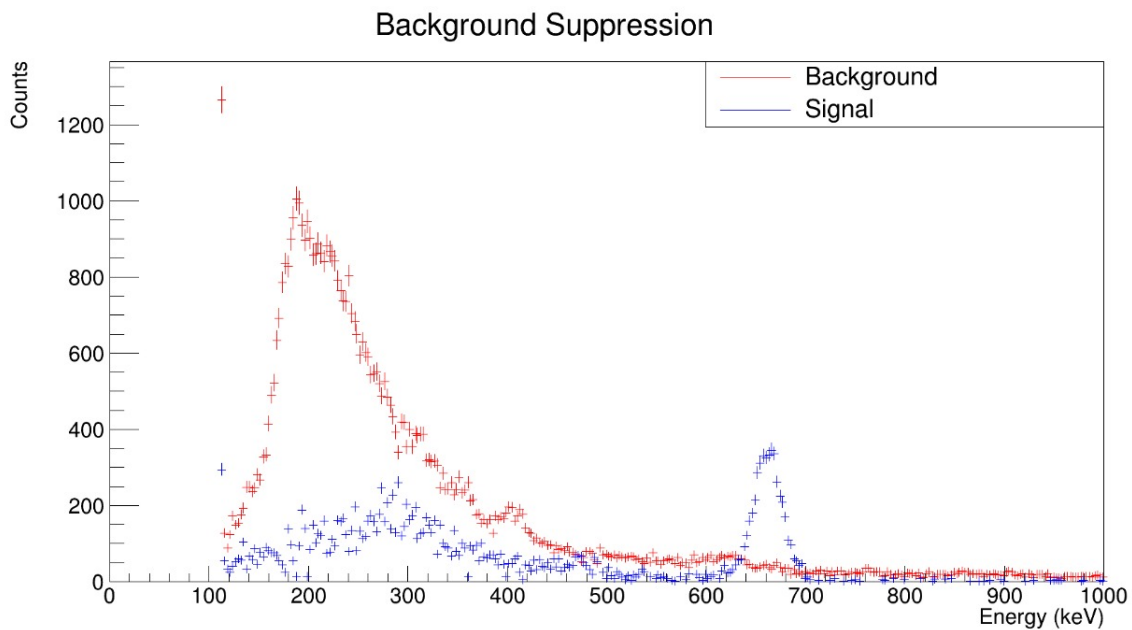
Figure 5.12: ^{137}Cs spectrum recorded for radionuclide identification with the UGV speed of 6.8 cm/s. The histogram in red markers shows the background while the one in blue markers represents the gamma spectrum after suppression of the background.

It can be clearly seen that the photopeak is located at 661.6 keV confirming the photopeak of ^{137}Cs.

Therefore, this leads to the confirmation of the radionuclide ^{137}Cs which is constituting the hotspot.

Conclusively, the UGV prototype consisting our detection system is able to detect both the radiation hotspot and the identification the radionuclide which comprises the hotspot. Therefore, the two prime objectives of the CLEANDEM were addressed successfully. However, the accuracy in the detection of the hotspot depends on the speed of the UGV and the shift should taken into account during the analysis procedure. Another factor is we are using an inorganic scintillator, NaIL which in general have a slower response than the organic scintillators. Therefore, similar tests should be performed using EJ-309 detection system for a comparative study. The identification system of the radionuclide is also working well and further tests need to be performed for gamma/neutron sources like Am-Be. The ^{252}Cf which is also a gamma/neutron source was not strong enough to perform the tests while maintaining a distance of 1 metre away from the source. Therefore, further tests need to be performed with stronger sources.

Chapter 6

Conclusion & Outlooks

This thesis work presents a study and characterization of two detection systems in the scope of CLE-ANDEM project. The two detectors used in this project work were an inorganic scintillator NaIL (size 2"x2") and an organic liquid scintillator EJ-309 (size 2"x2"). Both of these detectors have the gamma/neutron discrimination capability. These two detectors complement each other as NaIL can be used for gamma spectroscopy owing to its high resolution 6.5 % at 661 keV while EJ-309 can be used as a counter for gamma and neutrons due to its fast response.

The characterization of NaIL was focused on performing a gamma energy calibration and the determination of other important features of the detection system like energy resolution, gamma efficiency, and the pulse shape discrimination (PSD) between photons and thermal neutrons.

Preliminary studies were performed for EJ-309 which included its gamma energy calibration and pulse shape discrimination between photons and fast neutrons. The preliminary studies also consisted of comparison between EJ-309 cell coupled with 4x4 NUV SiPM array and EJ-309 coupled with HAMA-MATSU H-1949-51 PMT. While the EJ-309 coupled with SiPM promises to make the detection system compact, faster and consumes less power, however the difference in geometries between the SiPM and EJ-309 cell lead to the leakage of the scintillation light. This eventually contributed to the poor resolution of the detection system. Moreover, a parameter known as FoM which determines how well the gamma and neutrons are discriminated was found to be better for EJ-309 coupled to PMT 2.36 while for SiPM it was found to be 1.34.

Therefore, EJ-309 coupled to PMT proved to better detection system for further tests as a counter.

The ability of NaIL to discriminate gamma and thermal neutrons is exceptionally well with FoM = 4.10. NaIL was used as a thermal neutron counter in order to determine the best material to be used as a moderator. This test was performed in the scope of CLEANDEM project where there is high background radiation consisting of fast neutrons. In this situation, a moderator material needs to be used to detect the thermal neutrons. Three materials Graphite, Teflon and Polyethylene with different thickness were used as a moderator. ^{252}Cf was used a neutron source and the maximum number of neutrons were detected with Polyethylene having a thickness of 6 cm. Hence, polyethylene can be used as a moderator material for NaIL.

Further to address the main objectives of the CLEANDEM project which are remote localization of the hotspot and radionuclide identification, a UGV prototype was assembled with the detection system mounted on it. The detection system comprised of NaIL detector and STEMLAB Red-Pitaya digitizer which makes the detection system compact and faster. NaIL was found to be successful for hotspot localization as well as for radionuclide identification. The tests were performed at different speeds of the UGV and an optimal speed range of around 7 cm/s - 10 cm/s was determined at which the accuracy for the localization of the hotspot is well within 1 metre (100 cm).

Furthermore, another key objective of the CLEANDEM is to lower the human exposure to radiation by online dose-rate monitoring. With the motivation to address this objective, a study was performed to determine the Ambient dose rate, H*(10) using the gamma-spectra obtained from NaIL. The experiment is mentioned in detail in the appendix 7.1. While the conversion of gamma-spectra into ambient dose using stripping matrix is an interesting and clever approach however, the higher values of dose-rate were not very well determined by the NaIL detector of 2"x2" size. Therefore, NaIL cannot be used for ambient dose-rate estimation using gamma-spectra.

Further tests in the scope of the CLEANDEM project comprises of using a neutron source like Am-Be for hotspot localization and radionuclide identification. Once, the detection system is established for both the gamma and neutron radionuclides, the tests can be performed in different geometries in order to study the accuracy in the localization of the hotspot. Moreover, NaIL can then be replaced by EJ-309 coupled with the H-1949-51 PMT as a gamma and neutron counter for remote localization of the hotspot.

Chapter 7

Appendix

7.1 A-1:Ambient Dose H*(10)

For the purposes of routine radiation protection, it is better to represent a person's potential radiation exposure in terms of a single dose equivalent quantity that would exist in a phantom that closely mimics the human body. The chosen phantom is an object known as an ICRU (International Commission on Radiation Units) sphere, which is made of polymers with a diameter of 30 cm and a density of 1 g/cm^3 with a mass composition of 76.2%oxygen, 11.1% carbon, 10.1% hydrogen, and 2.6% nitrogen.The "ambient dose equivalent", H*(d), at a point in a radiation field is the dose equivalent that would be produced by the corresponding expanded and aligned field at a depth d in ICRU sphere, on the radius opposing the direction of the aligned field. The fluence, together with its directional and energy distribution, in an expanded field has the same values throughout the volume of interest as it does in the field itself at the point of reference. Additionally, the fluence must be unidirectional in order to have an extended and aligned radiation field. It is advised to use a reference depth, d, of 10 mm for strongly penetrating radiations [2].

7.1.1 Ambient Dose estimation H*(10) from NaIL Spectra

One of the prime objectives of the CLEANDEM project is to develop and exploit the technologies which can be embedded on Unmanned Ground Vehicle (UGV) to enable the full remote non-destructive characterization in harsh environments which involves remote hotspot localization using the detectors mounted on UGV while reducing human exposure to radiation. The two primary objectives of the CLEANDEM project hotspot localization and radionuclide identification were successfully addressed. Another objective of the CLEANDEM is dose-rate monitoring in order to reduce human exposure to radiation. Therefore, NaIL was further tested in order to calculate the Ambient dose, H*(10) using gamma-ray spectra obtained from NaIL. This work was inspired from [8, 38].

For detectors like high-purity Germanium (HPGe), the stripping method for ambient dose estimate has been applied. With this technique, the partial gamma ray absorptions made in the detector are removed from the spectrum, leaving just the events corresponding to a gamma ray's complete absorption. This approach is used in this work to acquire both the partial absorptions and the detector's complete peak efficiency on a 2"x2" NaIL detector. A Geiger counter and a NaIL detector were used to record the gamma spectrum after the stripping matrix had been created. The gamma spectrum was afterwards converted to ambient dose equivalent H*(10) for comparison with the Geiger counter. The derived H*(10) values from the NaIL detector are in good agreement with smaller values of dose measured by the Geiger counter. The various possible reasons of the deviations for the bigger values of dose derived from the spectra is also discussed at the end of the section.

7.1.2 Introduction

NaIL detectors are scintillation crystals with a good energy resolution, i.e. at 662 keV $\sim 7\%$. Therefore, in this test we used them for monitoring environmental radioactivity. Some countries such as Finland have started equipping their external monitoring stations with $LaBr_3$ detectors which have a resolution at 662 keV $\sim 3\%$ [35].

A gamma spectrometry monitor needs ambient gamma flux to determine H*(10). The observed gamma spectrum, however, does not account for the ambient gamma flux because of partial detector absorptions. To acquire the entire incident gamma, we need to determine the full peak energy efficiency. The *stripping method* refers to the process of removing all of these partial absorptions from the spectrum to leave only the counts resulting from full absorptions.

There are still technical challenges to be solved, though. Since the photomultiplier tube is temperature-sensitive, the energy calibration must be adjusted in accordance with the energy channel shift caused by temperature variations in order to operate this device automatically.

The limited availability of gamma energy sources restricts the experimental investigation of the detector response. However, as long as the detector geometry has been correctly established, Monte Carlo simulations permit the use of any energy and source. Geant4 was the Monte Carlo code employed in this project.

7.1.3 Methodology

In order to obtain only full absorptions, the stripping method involves removing all partial absorptions generated in the detector from the experimental spectrum. After the spectrum has been stripped, the external ambient flux and subsequent absorbed dosage are estimated using the full peak energy efficiency. Therefore, the only necessary knowledge for this method is the detector geometry; no external parameters are required.

Since the angular ambient flux is unknown, the detector response must be isotropic in order to apply the stripping approach in a straightforward and accurate manner. As a result, the methodology is divided into two sections:

1. Characterisation of the partial absorptions in the detector;

2. The application of the stripping method.

7.1.4 Experimental Setup

Having explained the methodology, this section discusses the experimental setup for performing the measurements. The Geiger counter which was used to measure the different doses, the sources used and how the dose rate was varied is also discussed. Since, the laboratory was not specially equipped for dose rate measurements, the geometrical accuracy was a bit compromised and the optimal configurations possible were used. The setup consisted of a Geiger counter, radioactive sources, NaIL detector, CAEN DT5725 digitizer, and a high voltage supply. Figure 7.1 shows the picture of experimental setup as configured in the laboratory.
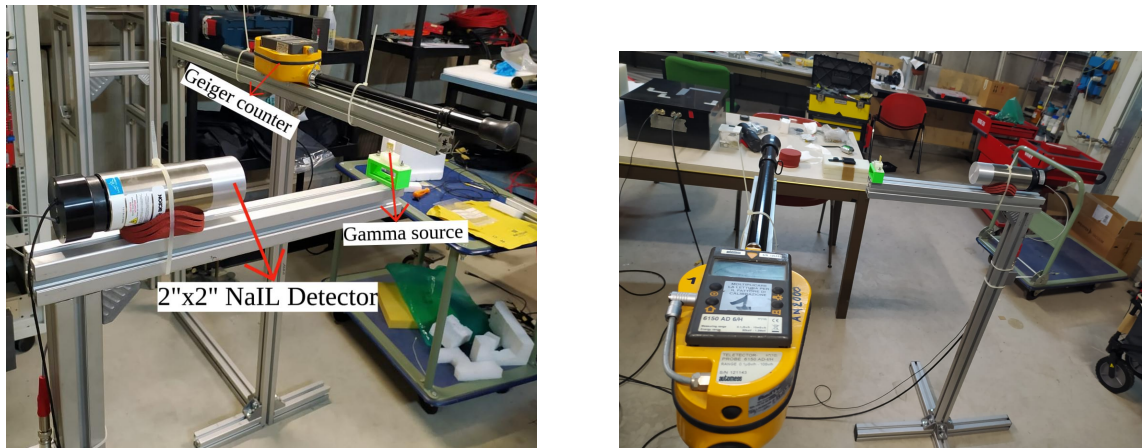
Figure 7.1: Experimental setup for dose rate measurement. Figure on left is labeled with different apparatus involved in measurements, while the figure on right shows the view of the configuration from the other side. It is important to notice the distance between the arm of the the Geiger counter and the source is equal to that between the source and the NaIL detector. This is to make sure that both the Geiger counter and NaIL are exposed to the same amount of radiation as the source is isotropic.

After placing the source in source tray, the distance between the arm of the Geiger counter and detector was measured, the source was then placed between the Geiger counter and detector at the middle point. In order to change the dose rate, the source was moved closer or farther from the Geiger counter depending on whether to increase or decrease the incoming dose respectively. The detector was then moved accordingly maintaining the equal distance between the source and the Geiger counter. The Geiger counter had measuring range from 0.1μSv/h to 10mSv/h and an energy range from 60 keV to 1.3 MeV which was also considered for the NaIL spectra. Figure 7.2 shows the Geiger counter that was used in the laboratory.

Figure 7.2: Geiger counter

7.1.5   Stripping Matrix

The following steps are a description of how to calculate the partial absorptions generated in the detector for various energy fluxes: [38]

1. A plane-parallel source is used for simulations. With a radius big enough to encompass the entire detector, the source is situated in front of the detector window. Since only scatterings

produced by the detector need to be stripped, simulations are run in a vacuum. For each energy bin in the experimental spectrum, simulations are mono-energetic.

2. According to the FWHM, the recommended bin width is around 5 keV channel^{-1} [36]. Energy bins that are excessively wide result in poor resolution, whereas energy bins that are too small necessitate performing many more simulations due to the need to simulate each bin. Additionally, tight bins in the measured spectra may result in poor statistical counts. For these reasons, the energy bin used in this work is 50 keV, both for simulations and measured spectra as proved by the study [37].

3. Normalisation of the simulated counts in each energy bin with the total counts detected in the photopeak was done in order to calculate the *(counts detected/ counts detected in the photopeak* ratio. In this way the simulated spectra are explained by the following vector:

$$\left(c_{j,1} = \frac{C_{j,1}}{C_{j,j}}, c_{j,2} = \frac{C_{j,2}}{C_{j,j}}, ..., c_{j,j-1} = \frac{C_{j,j-1}}{C_{j,j}}, c_{j,j} = \frac{C_{j,j}}{C_{j,j}} = 1 \right) \tag{7.1}$$

where $c_{j,i}$ are normalised scattered counts (partial absorptions) in the bin i produced by a photon with an energy corresponding to bin j, i.e the photopeak. $C_{j,i}$ are the same scattered counts before any normalisation.

4. Different spectra are organised in a matrix which is called the stripping matrix ($S_{j,i}$). These vectors contain information about the partial absorptions produced by each flux of energy j.

$$S_{j,i} = \begin{pmatrix} c_{n,1} & c_{n,2} & ... & c_{n,n-1} & 1 \\ c_{n-1,1} & c_{n-1,2} & ... & 1 & 0 \\ ... & ... & ... & ... & ... \\ c_{2,1} & 1 & ... & 0 & 0 \\ 1 & 0 & ... & 0 & 0 \end{pmatrix} \tag{7.2}$$

7.1.6 Dose rate calculation with the stripping method

Following is a description of the steps involved in obtaining the stripping spectra and, consequently, estimating the flux and dosage rate:

1. The detector's energy calibration needs to be performed frequently because the channel position is temperature dependent.

2. In the instance of 50 keV, the energy bin width of the experimental spectrum must be fitted with the simulated spectra.

3. Iteratively applying the equation 7.3 strips the experimental spectrum. This method of stripping goes from the highest energy bin to the lowest one.

$$C_i' = C_i^{exp} - \sum_{j=i+1}^{n} C_j'.S_{j,i} \tag{7.3}$$

where C_i' are the counts in an energy bin due to the total absorption of incident gamma flux, C_i^{exp} are the counts measured in this energy bin in the experimental spectrum and $S_{j,i}$ is the stripping matrix.

It is crucial to note that this iterative subtraction may result in negative counts. In these situations, they have been treated as 0 before the subsequent iteration.

4. Applying the following equation, counts in each energy bin of the resulting spectrum can be changed to incident flux:

$$\varphi_i = \frac{C_i'}{\varepsilon_i.t} \tag{7.4}$$

where ε_i is the energy efficiency in this energy bin obtained from previous Monte Carlo simulations and t is the spectrum measured time.

5. Estimate the H*(10) (μSv h^{-1}) from the incident flux rate, with equation 7.5.

$$H^*(10) = 1.6 * 10^{-10} \sum_{i=1}^{n} F_i.\varphi_i.E_i.\mu_i^{air} \tag{7.5}$$

where F_i is the conversion factor from the absorbed dose to the ambient dose, E_i is the energy of this energy bin (eV) and μ_i^{air} is the mass absorption coefficient for air (cm^2 g^{-1}).

7.1.7   Simulations

In order to construct the Stripping matrix, simulations needed to be performed from 50 keV to 2000 keV with the energy band cap of 50 keV making the total number of simulations 40. As mentioned in section 7.1.5, the simulations were performed in vacuum.

7.1.8   Analysis

Once the measurements were performed, the first step consisted of calculating the dose as measured by the Geiger counter. The reading in Geiger counter was taken over a period of 30 seconds. The counter's reading was changing almost every second, therefore in order to estimate the exact dose, a video recording of 30 seconds was taken for each measurement and then the average of the value was then taken. Table 7.1 represents the dose in μSv h^{-1} for the different measurements with the different gamma sources used.

Table 7.1: Ambient dose H*(10) measured by the Geiger counter and the different sources used.

H*(10) (μSv h^{-1})	Standard Deviation	Gamma Source
1.33	0.17	Cs-137
5.83	0.4	Cs-137
0.50	0.07	Cs-137
1.30	0.22	Co-60
1.83	0.20	Co-60
5.75	0.40	Co-60
2.26	0.27	Cs-137 + Co-60
9.85	0.30	Cs-137 + Co-60
18.13	0.66	Cs-137 + Co-60 + Na-22
0.77	0.09	Na-22
0.1	0.06	Background

The next step towards the long and iterative calculations was the energy calibration of NaIL. The different sources used were ^{137}Cs, ^{60}Co, and ^{22}Na. The calibration curve obtained is shown in figure 7.3. The temperature at the time of measurement was 42°C.
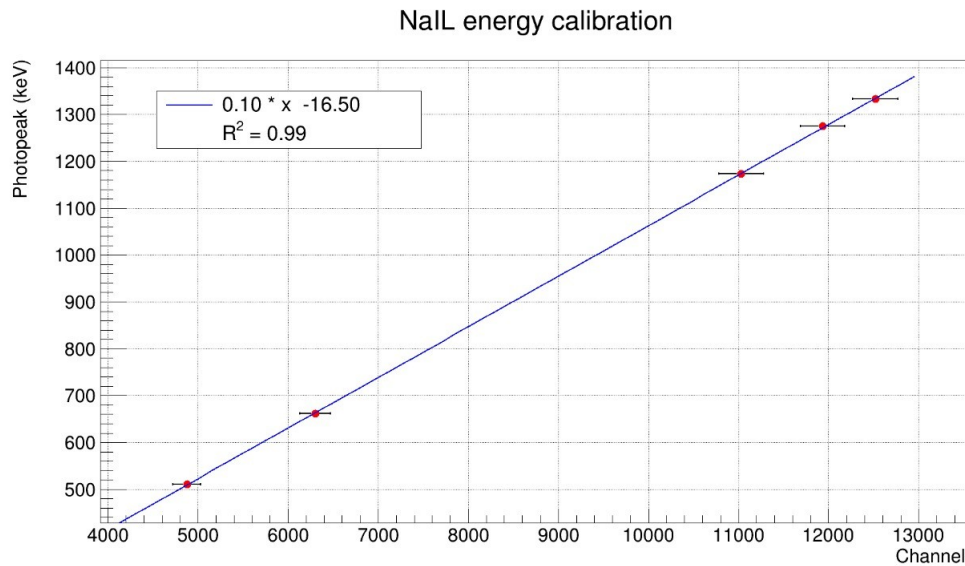
Figure 7.3: NaIL gamma energy calibration curve.

Once the calibration was done, the different spectra recorded were analysed. In order to obtain the counts in the interval of 50 keV, a for loop was written in the C++ macro which calculated the counts for every 50 keV interval until 2000 keV. The important point to be considered is that the counts were taken from 50 keV and not 0 keV as the Geiger counter's energy threshold is 60 keV.

Once, the counts were obtained for energy bin, the equation 7.3 was performed iteratively starting from 2000 keV energy bin to strip the experimental spectrum.

The next step was to determine the incident flux using equation 7.4. The time measured for spectrum was converted into hour. Once, the incident flux was obtained for each energy bin, the final step was to determine the ambient dose H*(10). In order to calculate this quantity, the conversion factor, F_i from the absorbed dose to the ambient dose was taken from [41]. μ_i^{air} which is the mass absorption coefficient was referred from [40]. Once these values were obtained, the ambient dose can then be easily calculated using equation 7.5.

7.1.9 Results

Irradiations of the NaIL detector was carried out in the laboratory. Different well-known values of the H*(10) were produced in the lab with ^{137}Cs, ^{60}Co, and ^{22}Na sources at different distances and so the stripping method was applied to the spectra provided by the detector. The results were then checked with known H*(10) values.

Table 7.2: Doses obtained from the NaIL spectra in the laboratory compared with nominal values.

Measured H*(10) (microSv/h)	Estimated H*(10) (microSv/h)	Relative difference(%)
0.1	0.05	-52.9
0.5	0.56	12.92
0.77	0.84	9.03
1.3	0.83	-36.15
1.33	1.43	7.5
1.83	1.37	-25.13
2.26	1.8	-20.31
5.75	3.38	-41.21
5.83	4.59	-21.26
9.85	3.86	-60.81
18.13	9.69	-46.58

H*(10) irradiated in this experiment were 0.1, 0.5, 1.3, 1.8, 2.3, 5.8, 9.9 and 18.1 µSv h^{-1} and the estimations calculated with the stripping method are shown in table 7.2. All H*(10) obtained with the stripping method were calculated with the 50 keV energy bin width. It can be seen the estimated value for smaller H*(10) doses are a bit overestimated. While for the bigger values of H*(10), the estimation is off by 50 % and needs a revision. For certain doses in the range of 1-2 µSv h^{-1}, the calculated dose is close to the measured dose while in some cases in the same range, it is under-estimated. This can be explained by the geometrical inaccuracy of the experimental setup. The laboratory is not well equipped for these measurements and a better experimental can be setup by trying different configurations.

7.1.10   Discussions

In this work the stripping methodology was derived from [38] and applied to experimental cases for 2"x2" NaIL detector. This methodology includes a process for deriving the fluence from gamma-ray spectra as well as the calculation of the fluence to H*(10) conversion factor. Geant4's Monte Carlo simulations were used to carry out the calculations.

The technique was used in a NaIL detector, and the H*(10) values that were produced were compared to the readings from a GM dosimeter. According to the findings, a more thorough inter-comparison study has to be conducted. The underestimation for smaller values of doses and over-estimations for the larger doses obtained from the gamma-ray spectra of NaIL can be explained by the limitation in geometrical configuration of the experimental setup or by the size of the NaIL crystal. Therefore, the tests need to be performed with better experimental configuration in the geometry and with higher accuracy in order to rule out the various variables leading the under and over-estimations.

Finally, this approach can be modified to obtain the H*(10) during the D&D operations in the CLE-ANDEM project not only for the NaIL detector but also for other types of spectrometric detectors, detectors made of different materials, detectors of various sizes, and calculations can be done for other gamma-ray energy ranges.

7.2   A-2: Uncertainty in FoM

As discussed in section 2.2.4 where the FoM is discussed in detail, assuming the Gaussian shape for both the gammas and the neutrons, the equation for FoM can further be modified using equation 2.3 which takes the form in case of inorganic scintillator like NaIL as:

$$\text{FoM} = \frac{\mu_{\text{neutron}} - \mu_{\gamma}}{2.35 * (\sigma_{\text{neutron}} + \sigma_{\gamma})} \qquad (7.6)$$

where µ is the mean of the Gaussian fit for both neutrons and gammas while σ is the standard deviation.

Furthermore, In order to incorporate the uncertainty in the calculated FoM, using error propagation for equation 7.6, the formula for uncertainty in FoM becomes:

$$\text{FoM} = \frac{(\mu_{\text{neutron}} \pm \Delta\mu_{\text{neutron}}) - (\mu_\gamma \pm \Delta\mu_\gamma)}{2.35 * (\sigma_{\text{neutron}} \pm \Delta\sigma_{\text{neutron}} + \sigma_\gamma \pm \Delta\sigma_\gamma)} = \frac{\mu \pm \Delta\mu}{2.35 * (\sigma \pm \Delta\sigma)} \tag{7.7}$$

$$\Delta\mu = \sqrt{(\Delta\mu_{\text{neutron}})^2 + (\Delta\mu_\gamma)^2} \tag{7.8}$$

$$\Delta\sigma = \sqrt{(\Delta\sigma_{\text{neutron}})^2 + (\Delta\sigma_\gamma)^2} \tag{7.9}$$

$$\left(\frac{\Delta\text{FoM}}{\text{FoM}}\right)^2 = \left(\frac{\Delta\mu}{\mu}\right)^2 + \left(\frac{\Delta\sigma}{\sigma}\right)^2 \tag{7.10}$$

$$\Delta\text{FoM} = \text{FoM}\left(\sqrt{\left(\frac{\Delta\mu}{\mu}\right)^2 + \left(\frac{\Delta\sigma}{\sigma}\right)^2}\right) \tag{7.11}$$

where $\mu = \mu_{\text{neutron}}$ - μ_γ and $\sigma = \sigma_{\text{neutron}} + \sigma_\gamma$ while Δ stands for uncertainty in the quantities like µ,σ and FoM.

7.3   A-3: EJ-309 coupled to PMT

For the comparative study of EJ-309 coupled with SiPM, the calibration and gamma/neutron discrimination was also done for EJ-309 coupled with PMT. In this section, the same tests and analysis was performed as for EJ-309 coupled with SiPM. In the end, the resolution and FoM values are compared for both the combination of the detection system.

7.3.1   Calibration

By allocating each gamma-Compton ray's edge energy to the channel where the amplitude of the Compton plateau reaches 80% of its maximum intensity, the EJ-309 detector was calibrated. [27]. Figure 7.4 represents the spectrum of ^{22}Na of the EJ-309 2"x2" using the CAEN digitizer DT5725 and PMT model Hamamatsu H1949-51 PMT without the energy calibration (counts vs channel) where two Compton edges of the ^{22}Na can be seen, and the two points used for the calibration are indicated.
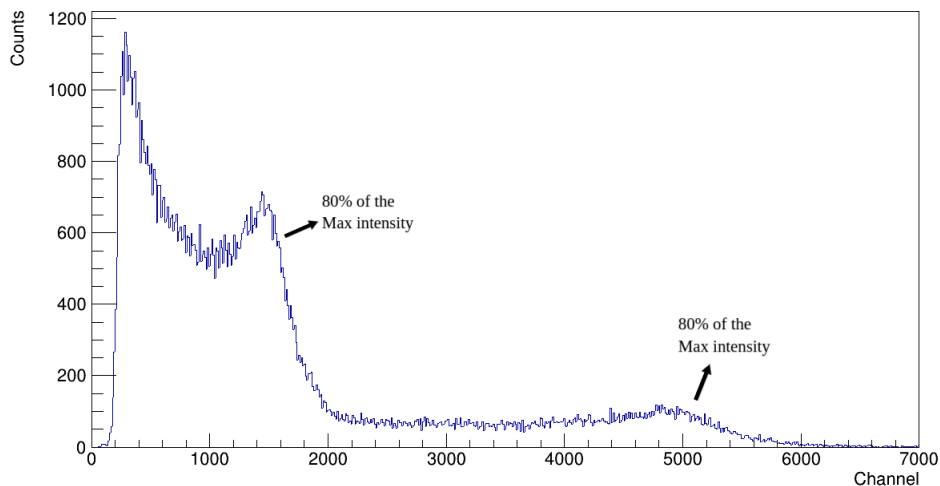

Figure 7.4: Energy spectrum of the ^{22}Na without the energy calibration, using the EJ-309 coupled with PMT.

Figure 7.5 shows the calibration curve of EJ-309 with SiPM. The different gamma sources used were ^{137}Cs, ^{60}Co and ^{22}Na. The two Compton edges of ^{60}Co cannot be seen due to limitation in the resolution of the EJ-309 scintillator. Therefore for calibration purpose, the average energy of the two Compton edges was taken.
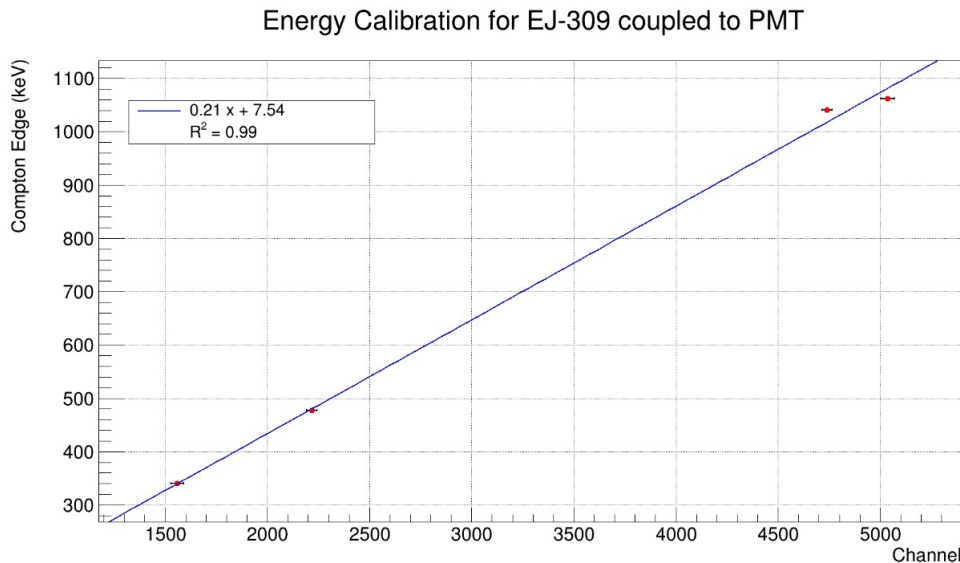

Figure 7.5: Gamma energy calibration of the 2"x2" EJ-309 cell coupled to PMT with DT5725 digitizer.

7.3.2   Optimization of fast neutron and gamma discrimination

The parameters of the digitizers had to be optimized in order to get the best response for the neutron/gamma discrimination capabilities of the EJ-309 detector, as discussed in subsection 4.2.2. A neutron-gamma source of ^{252}Cf was used with CAEN DT5725 digitizer. The measurement with neutron-gamma source ^{252}Cf was carried out for around 16 minutes to have better counts. Waveforms that had been digitally processed and recorded throughout the measurement were each given an acquisition window of about 4 ns.

To optimize the integration windows, an offline study similar to the one carried out for the EJ-309 in combination with SiPM was conducted. Figure 7.6 illustrates the energy spectrum of all the events that have energies between 900 keVee and 1400 keVee. The Compton edge associated with the gamma-ray energy of 1274.537 keV (^{22}Na) is represented by this choice.

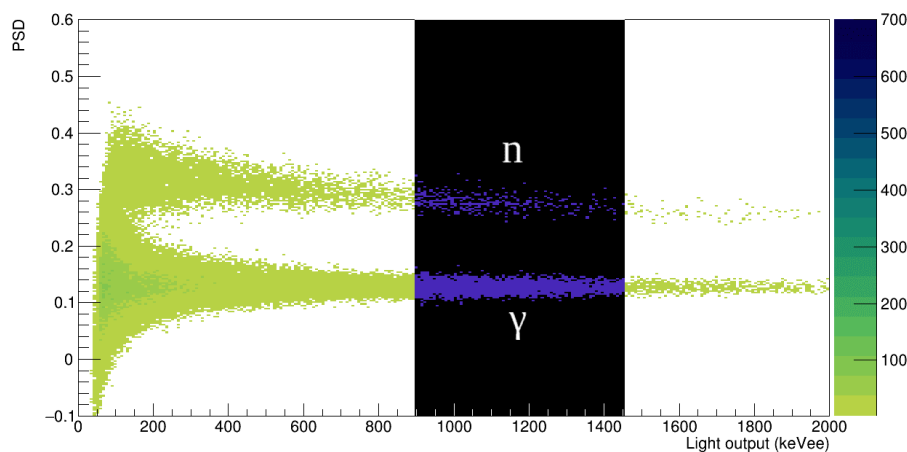Figure 7.6: Pulse shape discrimination parameter versus energy for ^{252}Cf source for EJ-309 coupled with PMT. The black strip indicates the energy region used for PSD optimization. For the energy calibration we used gamma sources, therefore keVee (kilo electron Volt electron equivalent) as the unit of measurement of energy is used.

As seen in figure 7.7, the events in this energy range are plotted as a function of PSD, and the FoM is then calculated by performing two Gaussian fittings of the neutron and gamma events. For the measurement, the pregate and pretrigger were set at 10 and 100 nanoseconds, respectively. For EJ-309 paired with PMT, the optimal value of the FoM was discovered to be 2.34 ± 0.03. For the equivalent FoM, Q_{long} and Q_{short} have respective values of 150 ns and 17 ns.
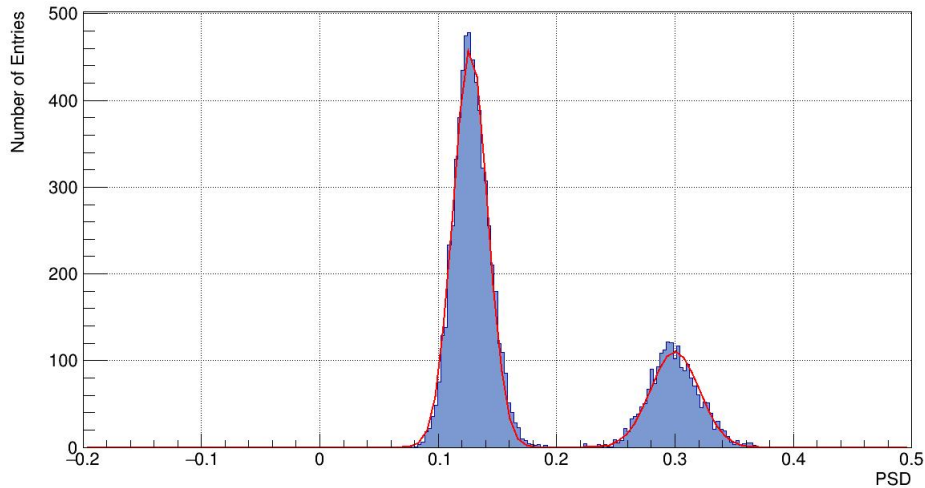

Figure 7.7: Gaussian fit for the gamma (left) and the neutron (right) to calculate the FoM for EJ-309 coupled to PMT. Corresponding FoM = 2.34.

Bibliography

[1] Knoll G. Radiation detection and measurement. 4th ed. New York: Wiley; 1979.

[2] Leo W. Techniques for nuclear and particle physics experiments. 2nd ed. Berlin: Springer-Verlag; 1994.

[3] https://www.crystals.saint-gobain.com/radiation-detection-scintillators/crystal-scintillators/nail-scintillation-crystals [cited on 31/07/2022].

[4] Siegel, Peter; Eskandari, Sephir. "Introduction to Geiger Counters" https://www.cpp.edu/ pb-siegel/bio431/texnotes/chapter4.pdf [cited on 31/07/2022]

[5] Marques L, Vale A, Vaz P. State-of-the-Art Mobile Radiation Detection Systems for Different Scenarios. Sensors. 2021;21(4):1051.

[6] Special Nuclear Material [Internet]. NRC Web. 2021 [cited 23 July 2021]. Available from: https://www.nrc.gov/materials/sp-nucmaterials.html

[7] Incident and Trafficking Database (ITDB) — IAEA [Internet]. Iaea.org. 2021 [cited 23 July 2021]. Available from: https://www.iaea.org/resources/databases/itdb

[8] Calculation of the ambient dose equivalent H*(10) from gamma-ray spectra obtained with scintillation detectors, https://www.sciencedirect.com/science/article/pii/S0969804316303268

[9] Brunelli D, Pino F, Fontana C, Pancheri L, Moretto S. DRAGoN: Drone for Radiation detection of Gammas and Neutrons. 2020.

[10] User S. EJ-276 - Pulse Shape Discrimination Plastic Scintillator - Eljen Technology [Internet]. Eljentechnology.com. 2021 [cited 1 April 2021]. Available from: https://eljentechnology.com/products/plastic-scintillators/ej-276

[11] Detection R, Scintillation C, Materials C, (Ce)] C. CLLB — Products — Saint-Gobain Crystals [Internet]. Crystals.saint-gobain.com. 2021 [cited 23 July 2021]. Available from: https://www.crystals.saint-gobain.com/products/cllb

[12] Red Pitaya STEMlab board [Internet]. Redpitaya.com. 2021 [cited 14 June 2021]. Available from: https://www.redpitaya.com/f130/STEMlab-board

[13] CAEN - Tools for Discovery [Internet]. CAEN - Tools for Discovery. 2021 [cited 14 June 2021]. Available from: https://www.caen.it/

[14] User S. Home - Eljen Technology [Internet]. Eljentechnology.com. 2021 [cited 14 June 2021]. Available from: https://eljentechnology.com/

[15] ASD-RGB4S-P-4x4TD, ASD-NUV4S-P-4x4TD [Internet]. Advansid.com. 2021 [cited 8 June 2021]. Available from: https://advansid.com/products/product-detail/asd-sipm4s-p-4x4td

[16] Birks J. B. The Theory and Practice of Scintillation Counting. Pergamon Press Ltd., 1st Edition, 1964.

[17] Pino F. Development of Innovative Technology for Detection and Identification of Radioactive Materials. PhD Thesis, Univerity of Padova; 2014.

[18] SensL. Introduction to SiPM. 2017.

[19] Acerbi F, Gundacker S. Understanding and simulating SiPMs. Nuclear Instruments and Methods
      in Physics Research Section A: Accelerators, Spectrometers, Detectors and Associated Equipment.
      2019;926:16-35.

[20] Pino F, Delgado J, Mantovani G, Pancheri L, Fabris D, Fontana C et al. Novel neutron detector
      assembly based on SiPM readout to be coupled with the Active Target for SPES.

[21] Stevanato L, Fabris D, Hao X, Lunardon M, Moretto S, Nebbia G et al. Light output of EJ228
      scintillation neutron detectors. Applied Radiation and Isotopes. 2011;69(2):369-372.

[22] F. Pino, C. Fontana, D. Fabris, G. Nebbia, M. Turcato, D. Brunelli, L. Pancheri, A. Quaranta, S.
      Moretto. Characterization of a medium-size CLLB scintillator and its potential use in an unmanned
      airborne radiation monitoring system. 2020.

[23] Home [Internet]. Hamamatsu.com. 2021 [cited 14 June 2021]. Available from:
      https://www.hamamatsu.com/eu/en/index.html

[24] Cester D. Materials, instrumentation and techniques for the detection of Special Nuclear Material
      and Radioactive Sources: EU project MODES SNM. PhD Thesis, University of Padova.

[25] Fontana C, Carnera A, Lunardon M, Pino F, Sada C, Soramel F et al. A distributed data
      acquisition system for nuclear detectors. International Journal of Modern Physics: Conference
      Series. 2018;48:1860118.

[26] Agostinelli S. et al. Geant4 a simulation toolkit. Nuclear Instruments and Methods in Physics
      Research A, 506:250-303, 2003.

[27] Liao C, Yang H. Pulse shape discrimination using EJ-299-33 plastic scintillator coupled with a
      Silicon Photomultiplier array. Nuclear Instruments and Methods in Physics Research Section A:
      Accelerators, Spectrometers, Detectors and Associated Equipment. 2015;789:150-157.

[28] Nakamura K. [Internet]. Pdg.lbl.gov. 2021 [cited 12 August 2021]. Available from:
      https://pdg.lbl.gov/2011/reviews/rpp2011-rev-particle-detectors-accel.pdf

[29] Grodzicka-Kobylka M, Szczesniak T, Moszynski M, Brylew K, Swiderski L, Valiente-Dobon J
      et al. Fast neutron and gamma ray pulse shape discrimination in EJ-276 and EJ-276G plastic
      scintillators. Journal of Instrumentation. 2020;15(03):P03030-P03030.

[30] Krane K. Introductory nuclear physics. New York, N.Y.: Wiley; 1988.

[31] http://www.nucleide.org/Laraweb/index.php

[32] Determination of energy resolution for a NaI(Tl) detector modeled with FLUKA code Nuclear En-
      gineering and Technology,https://www.sciencedirect.com/science/article/pii/S1738573321002680

[33] Measurement   of   Compton   edge   position   in   low-Z   scintillators
      https://www.sciencedirect.com/science/article/pii/S1350448709001917

[34] Gamma-calibration of NE 213 scintillation countershttps://www.sciencedirect.com/science/article/pii/002955

[35] Research activities of STUK 2005 - 2010

[36] Gilmore, G. R. Practical Gamma-ray Spectrometry, second edn. John Wiley Sons, Ltd. (2008).
      ISBN: 978 0470861967.

[37] Ambient dose estimation H*(10) from LaBr3(Ce) spectra https://doi.org/10.1093/rpd/nct342

[38] Miller, K. M. A spectral stripping method for a Ge spectrometer used for indoor gamma exposure rate measurements. USDOE publication, EML-419 (New York: Environmental Measurement Laboratory) (1984).

[39] International Organization for Standardization.Calibration of an area and personal dosimeters and the measurement of their response as a function of energy and angle of incidence. ISO 4037-3. ISO (1999).

[40] https://physics.nist.gov/PhysRefData/XrayMassCoef/ComTab/air.html [cited on 08/07/2022].

[41] https://www.icrp.org/docs/ICRU%20Radiation%20Exposure.pdf

[42] The Californium-252 Fission Neutron Spectrum from 0.5 to 13 MeV, https://doi.org/10.13182/NSE73-A28979

[43] https://www.hamamatsu.com/eu/en/product/optical-sensors/pmt/pmt-assembly/head-on-type/H1949-51.html [cited on 04/10/2022]

[44] https://www.hamamatsu.com/eu/en/product/optical-sensors/pmt/pmt-assembly/head-on-type/H1949-51.html [cited on 04/10/2022]

[45] Determination of energy resolution for a NaI(Tl) detector modeled with FLUKA code, https://www.sciencedirect.com/science/article/pii/S1738573321002680